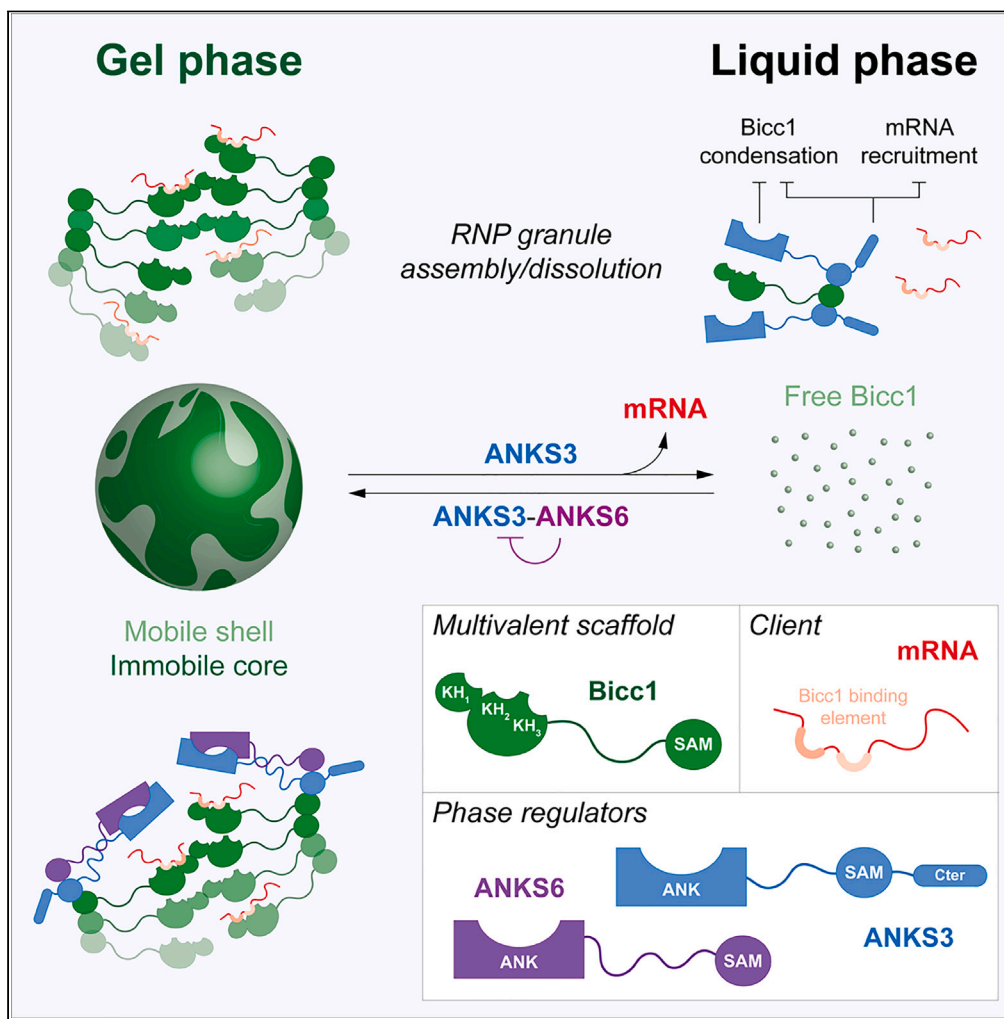**Article**

Antagonistic interactions among structured domains in the multivalent Bicc1-ANKS3-ANKS6 protein network govern phase transitioning of target mRNAs

Benjamin Rothé,
Simon Fortier,
Céline Gagnieux,
Céline
Schmuziger,
Daniel B. Constam

daniel.constam@epfl.ch

Highlights

Self-interacting KH domains remodel SAM domain-induced Bicc1 fibers in a 3D meshwork

Recruitment to Bicc1 granules confers gel-like behavior to client mRNAs

Specific ANKS3 domains independently revert Bicc1 condensation and mRNA recruitment

Co-recruitment of ANKS6 by ANKS3 can reinstate mRNA condensation by Bicc1 granules

Article

Antagonistic interactions among structured domains in the multivalent Bicc1-ANKS3-ANKS6 protein network govern phase transitioning of target mRNAs

Benjamin Rothé,[1] Simon Fortier,[1,2] Céline Gagnieux,[1] Céline Schmuziger,[1] and Daniel B. Constam[1,3,*]

SUMMARY

The growing number of diseases linked to aberrant phase transitioning of ribonucleoproteins highlights the need to uncover how the interplay between multivalent protein and RNA interactions is regulated. Cytoplasmic granules of the RNA binding protein Bicaudal-C (Bicc1) are regulated by the ciliopathy proteins ankyrin (ANK) and sterile alpha motif (SAM) domain-containing ANKS3 and ANKS6, but whether and how target mRNAs are affected is unknown. Here, we show that head-to-tail polymers of Bicc1 nucleated by its SAM domain are interconnected by K homology (KH) domains in a protein meshwork that mediates liquid-to-gel transitioning of client transcripts. Moreover, while the dispersion of these granules by ANKS3 concomitantly released bound mRNAs, co-recruitment of ANKS6 by ANKS3 reinstated Bicc1 condensation and ribonucleoparticle assembly. RNA-independent Bicc1 polymerization and its dual regulation by ANKS3 and ANKS6 represent a new mechanism to couple the reversible immobilization of client mRNAs to controlled protein phase transitioning between distinct metastable states.

INTRODUCTION

Liquid-liquid or liquid-gel phase separations can segregate molecules from their solute into supramolecular polymer condensates such as stress granules (SGs) and P-bodies (PBs) that participate in RNA metabolism and translational control.[1,2] Phase transitioning of SGs and PBs is nucleated by intrinsically disordered regions (IDRs) that cooperate with RNA-binding domains to assemble multivalent protein-protein and protein-RNA interaction networks. In addition, phase separation can be modulated by intermolecular RNA-RNA contacts, and by changes in pH, salinity, and temperature to allow rapid integration of environmental cues, and in a reversible manner.[1,3,4] Perturbations which instead favor irreversible aggregation are implicated in a growing number of diseases.[5]

PBs and SGs can accrue hundreds of proteins including Bicc1, an RNA-binding protein involved in post-transcriptional regulation of gene expression.[6–12] Protein interactome screening revealed that Bicc1 binds to eIF3A and eIF3B, which in stressed cells promote SG formation, and to the carbon catabolite repressor 4–negative on TATA (Ccr4-Not) complex, a component of PBs.[12–16] However, rather than entering PBs, Bicc1 forms distinct granules both in cultured cells and in mouse kidneys, as well as in *Drosophila* oocytes.[9,10,14] Bicc1 also does not overlap with SGs, except after global inhibition of mRNA translation by hippuristanol treatment.[8]

Bicc1 consists of a tandem repeat of three KH and two KH-like (KHL) domains that are separated from a self-polymerizing sterile alpha motif (SAM) by a disordered intervening sequence (IVS) (Figure 1A). The SAM domain is a widespread globular domain composed of two distinct surfaces called mid-loop (ML) and end-helix (EH), which mediate head-to-tail polymerization in helical arrangements.[17,18] In crystals, the SAM domain of Bicc1 forms a flexible polymer scaffold that is predicted to distribute the KH repeat at its periphery.[10,19] Loss of Bicc1 in vertebrates provokes the development of fluid-filled cysts reminiscent of polycystic kidney diseases (PKD).[20] Cyst formation in PKD kidneys depends on cAMP synthesis by adenylate cyclase 6 (Adcy6).[21,22] Bicc1 mutant kidneys accumulate cAMP in excess, correlating with de-repression of adenylate cyclase 6 (*Adcy6*) mRNA translation.[23] Mechanistically, *Adcy6* mRNA silencing by Bicc1 depends on KH domains to bind the 3′UTR, and on the SAM domain to concentrate the resulting Bicc1

[1]Ecole Polytechnique Fédérale de Lausanne (EPFL) SV ISREC, Station 19, 1015 Lausanne, Switzerland

[2]Present address: Molecular Genetics of Stem Cells Laboratory, Institute for Research in Immunology and Cancer (IRIC), Université de Montréal, Montreal, QC H3T 1J4, Canada

[3]Lead contact

*Correspondence: daniel.constam@epfl.ch
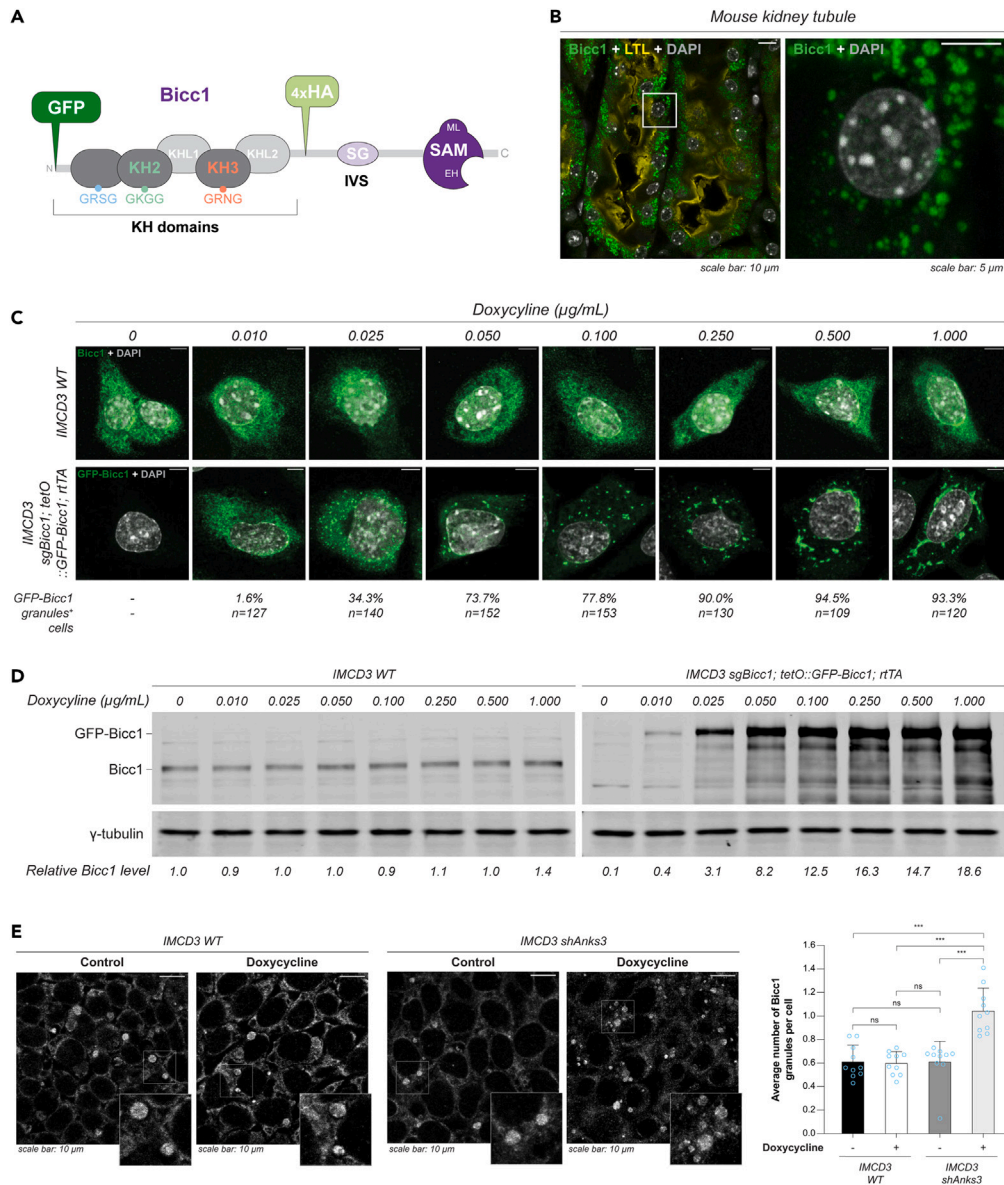https://doi.org/10.1016/j.isci.2023.106855

Figure 1. Granule formation by endogenous Bicc1 in mouse kidneys is recapitulated by HA-Bicc1 and GFP-Bicc1 in HeLa cells

(A) Illustration of Bicc1 protein domains and of GFP or 4xHA-tag insertion sites. KH and SAM domains are separated by a serine and glycine (SG)-rich intervening sequence (IVS). The GXXG motifs, where at least one X is arginine or lysine, orient four single-stranded nucleotides toward the RNA binding cleft of the KH domains. EH and ML surfaces link the SAM domain in head-to-tail polymers.

(B) Immunofluorescence staining of Bicc1 (green) in adult mouse kidney. Fluorescent LTL (yellow) marks proximal tubules. The boxed area is magnified in the panel to the right.

(C) Anti-Bicc1 staining of control IMCD3 cells (top) or CRISPR-edited IMCD3_sgBicc1 cells (bottom) treated with increasing concentrations of doxycycline to monitor the induction of a tetO::GFP-Bicc1 transgene by reverse Tet transactivator (rtTA). Scale bars, 5 μm. The percentage of cells exhibiting a granular GFP-Bicc1 pattern was counted in >100 cells from at least 5 areas of 200 μm^2 each using ImageJ software.

(D) Western blot analysis of endogenous Bicc1 and GFP-Bicc1 in cells treated as in (C). The levels of Bicc1 were normalized to γ-tubulin.

(E) Immunofluorescence staining of endogenous Bicc1 in IMCD3-shANKS3 cells treated with or without 0.25 μg/mL doxycycline to induce Anks3 shRNA. Insets: High magnification of Bicc1 granules. The average number of Bicc1 granules

Figure 1. *Continued*

per cell larger than 0.5 μm² and with a circularity threshold ≥0.5 was counted using ImageJ. Blue circles represent the individual values from 10 fields of view, each covering an area of 200 μm². Data are means +SD. ns: non-significant, *p < 0.05, **p < 0.01, ***p < 0.001 (Student's *t* test).

ribonucleoparticles (RNPs) in cytoplasmic granules.[10,23] In keeping with a role for SAM domain polymerization *in vivo*, a splice site mutation in the SAM domain that impairs granule formation in kidneys of Bicc1[bpk/bpk] mutant mice, or targeted mutagenesis of the self-polymerization interface of the SAM domain each abrogate the silencing of Bicc1-associated *Adcy6* mRNA.[10] In addition, loss-of-function studies in mouse and frog embryos revealed a role for Bicc1 in specifying the left-right asymmetry of visceral organs during embryogenesis.[9] In this process, an essential function of Bicc1 is to accelerate the decay of *Dand5* mRNA in response to flow stimulation of primary cilia.[24,25] *Dand5* mRNA is bound by the KH_1 and KH_2 domains of Bicc1 via a bipartite GAC motif in the conserved GACGUGAC sequence of the 3'UTR, leading to reduced expression on the left side of the node.[25] However, whether the assembly of Bicc1 RNPs or their dynamics are regulated is unknown.

Bicc1 forms a complex with ANKS3 and ANKS6 both *in vitro* and in mouse kidneys.[19,26–29] Mutations in ANKS6 associate with chronic kidney disease in nephronophthisis patients and perturb left-right patterning in animal models.[30–33] Depletion of ANKS3 increases the frequency of heart situs inversions in developing zebrafish embryos, and a variant of ANKS3 has been identified in a family with severe laterality defects.[29,34] Cell-free analysis established that the SAM domains of Bicc1, ANKS3, and ANKS6 can form highly ordered heterooligomers, with ANKS3 either capping the Bicc1 SAM domain or being sequestered by the SAM domain of ANKS6 to thereby limit or promote, respectively the polymerization of Bicc1/Anks3 complexes in an extended meshwork. This model was corroborated by reconstitution experiments in heterologous cells showing that ANKS3 disperses cytoplasmic Bicc1 granules, whereas the recruitment of ANKS6 by ANKS3 rescues the condensation of all three proteins in large condensates.[19] Importantly, the remodeling of Bicc1 polymers by the ANKS proteins involves additional structured domains, including an interface of at least the Bicc1 KH domains with ANKS3, and the C-terminal region of ANKS3 that disperses Bicc1 granules, presumably through steric hindrance of Bicc1 polymer extension.[19,28,35] In addition, ANKS3 and ANKS6 associate through their N-terminal Ank repeats.[19] The multivalent network of interaction between these proteins and overlapping phenotypes of their pathogenic variants suggest a shared function; however, whether and how these proteins regulate each other is unknown.

RNA granules are commonly nucleated by proteins with IDRs and RNA-binding domains, and are further modulated by protein-RNA and RNA interactions. By contrast, the condensation of Bicc1 and bound mRNAs mainly relies on well-structured protein domains. Here, we investigate the phase separation properties of Bicc1 RNPs and their regulation by ANKS3 and ANKS6, and the potential influence of known client mRNAs themselves. We show that the KH repeat contributes to phase separation, independently of bound RNA, by remodeling SAM domain-induced Bicc1 fibrils into a meshwork of gel-like granules exhibiting actomyosin-dependent mobility. Live imaging and high-resolution microscopy reveal the liquid-to-gel transitioning of bound-mRNAs in Bicc1 condensates and its dual regulation by ANKS3 and ANKS6. Our results highlight a new role of the N-terminal ankyrin repeat of ANKS3 in the emulsification of Bicc1 condensates by modulating the surface tension and the retention of bound mRNAs. Conversely, co-recruitment of ANKS6 rescues the condensation of Bicc1 and its target transcript. Taken together, our data suggest that ANKS3 and ANKS6 modulate the conformation of oligomeric Bicc1 to couple phase separation with RNA binding.

RESULTS

Bicc1 condensation in granules is dose-dependent and antagonized by *Anks3*

Previously, we and others have shown that Bicc1 demixes from surrounding cytoplasm to assemble micrometer scale granules both in cells and tissues,[10,14] regardless of the presence or absence of an N-terminal green fluorescent Ppotein (GFP) tag (GFP-Bicc1) or of a 4xHA epitope (HA-Bicc1) in the IVS between the KH repeat and the SAM domain (Figures 1A and 1B).[8,9,11,19] However, whether the condensation of Bicc1 is regulated and hence dose-dependent has not been tested. To address this, we introduced a doxycycline-inducible lentiviral GFP-Bicc1 transgene into CRISPR-edited IMCD3_sgBicc1 cells.[15] In parental IMCD3 control cells, endogenous Bicc1 formed widely distributed cytoplasmic puncta which rarely exceeded the size resolution threshold of 0.05 μm², and addition of doxycycline did not change this

distribution. GFP-Bicc1 induced by minimal concentrations of doxycycline (≤0.025 μg/mL) mimicked this localization at expression levels up to 3-fold above those of endogenous Bicc1 (Figures 1C and 1D). By contrast, above this threshold, GFP-Bicc1 phase separates in a few large condensates in the majority of cells (Figures 1C and S1A). This result indicates that the condensation of GFP-Bicc1 is dose-dependent, consistent with a process of phase separation. In addition, a rise in Bicc1 concentration may promote phase transitioning by titrating inhibitors of Bicc1 polymerization such as ANKS3.[19] To address this, we imaged endogenous Bicc1 condensates in an IMCD3 cell line expressing a validated doxycycline-inducible *Anks3* shRNA.[36] Since no antibodies were available to specifically detect ANKS3 protein, we confirmed by RT-qPCR that doxycycline administration depleted the *Anks3* mRNA by 85%. Concomitantly, the average frequency of Bicc1 condensates larger than 0.5 μm^2 increased by 71% from 0.61 to 1.05 per cell (n = 8, p < 0.001) (Figure 1E). Doxycycline treatment of control cells without *Anks3* shRNA did not alter the size of Bicc1 condensates. Together, these results suggest that the phase transitioning of endogenous Bicc1 in IMCD3 cells is limited both by its own concentration and by ANKS3.

Bicc1 granules can acquire actomyosin-dependent mobility

During live imaging, cytoplasmic GFP-Bicc1 condensates did not always remain stationary. Systematic tracking in time-lapse movies revealed saltatory movements and sporadic splitting and fusion events (Figures S1B and S1C). Treatment with the myosin II inhibitor blebbistatin or with the ROCK inhibitor Y27632 diminished the total distance traveled by individual GFP-Bicc1 granules by 40–50% (Figure S1D). The mobility of GFP-Bicc1 granules also decreased on average by $12.5 \pm 2.2\%$ upon treatment with the actin polymerization inhibitor cytochalasin D, and by $15.3 \pm 2.8\%$ after microtubule depolymerization by nocodazole. By contrast, treatment with the kinesin inhibitor monastrol had no effect. These observations suggest that Bicc1 condensates are eligible for cytoskeletal transport mediated by actomyosin and to a lesser extent by microtubules.

ANKS3 and ANKS6 modulate the association of Bicc1 with PBs

Bicc1 granules localize in close vicinity of PBs independently of the RNA-binding KH domains via polymerization of the SAM domain.[9,10] To test whether the effects of ANKS proteins on Bicc1 SAM domain polymerization correlate with an altered association with PBs, we stained HA-Bicc1 and ANKS3-Flag or V5-ANKS6 in HeLa cells expressing the PB marker GFP-DCP1a. In ANKS3-Flag positive cells, the clustering of Bicc1 around PBs was lost concurrently with its dispersal throughout the cytoplasm, whereas co-expression of ANKS6 rescued it (Figure S1E). These data corroborate the notion that PBs and Bicc1 condensates are interconnected by protein-protein interactions.

Bicc1 condensates in cell extracts depend on electrostatic interactions mediated by both the SAM and KH domains

To characterize Bicc1 RNP dynamics and their regulation by phase transitioning *in vitro*, we first expressed Bicc1 in *E. coli*. However, as the full-length protein remained insoluble and resisted purification, we switched to a protocol of differential centrifugation that enriches macromolecular condensates from mammalian cell extracts[37–39] (Figure 2A). In extracts of *Bicc1* wild-type IMCD3 cells, low-speed centrifugation enriched 27% of endogenous Bicc1 protein in heavy fractions (Figure 2B). A comparison with inducible GFP-Bicc1 in our engineered cell line revealed that sedimentation is dose-dependent and that the concentrations needed to enrich 30% of GFP-Bicc1 in heavy fractions was approximately 8-fold above the level of endogenous Bicc1, suggesting that the GFP-tag does not diminish Bicc1 solubility but rather increases it (Figure S2A). To test whether this sedimentation requires binding of Bicc1 to RNA, we treated cell extracts for 20 min with RNase A or pre-incubated them with a 442 nucleotide fragment of the proximal *Adcy6* 3′UTR that specifically binds to Bicc1 KH domains.[23] Neither treatment with RNase A nor addition of synthetic target RNA significantly altered GFP-Bicc1 sedimentation (Figure S2B). By contrast, addition of NaCl dose-dependently increased GFP-Bicc1 solubility, with complete solubilization being reached at ≥300 mM (Figure S2C). These results show that sedimentation of Bicc1 is reversible and apparently independent of mRNA, assuming that Bicc1 unlikely protects bound RNA against RNase. To validate this conclusion in an unrelated cell line, and to rule out a potential artifact of GFP, we also analyzed the sedimentation of HA-Bicc1 and of truncation mutants in extracts of transiently transfected HEK293T cells (Figure S3). Whereas 72% of overexpressed HA-Bicc1 partitioned to heavy fractions after low-speed centrifugation, deletion of either the SAM or the KH domains diminished the sedimented fraction by 12% or 57%, respectively (Figure 2C). These results suggest that the KH domains diminish Bicc1 solubility through reversible electrostatic interactions, at least *in vitro*.
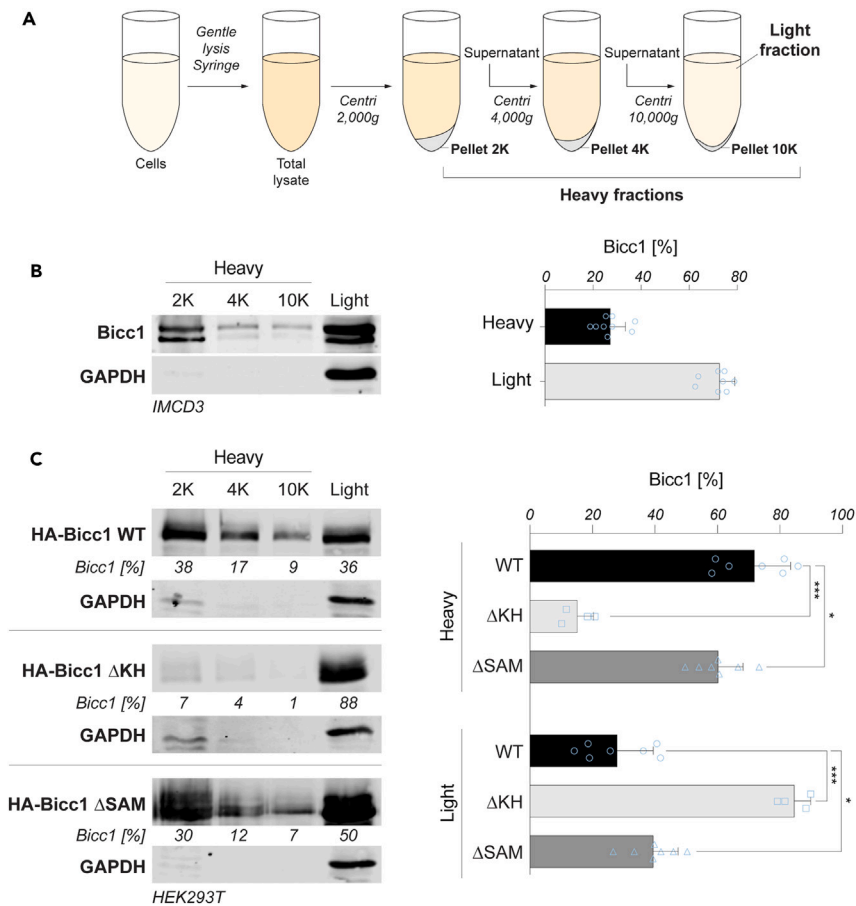
Figure 2. The KH domains promote Bicc1 sedimentation by low-speed centrifugation

(A) Procedure of cell fractionation by low-speed differential centrifugation.

(B) Western blot of IMCD3 cell extracts after stepwise centrifugation at 2,000, 4,000, and 10,000 g. The relative distribution of mBicc1 in heavy (2K, 4K, and 10K) versus light fractions is quantified on the right. Equal volumes of the indicated solubilized pellets and supernatants were analyzed. Data are means +SD from nine independent experiments.

(C) Sedimentation of HA-Bicc1 wild-type (WT), ΔKH, or ΔSAM by stepwise centrifugation of cell extracts of transiently transfected HEK293T cells as in (A). Data are means +SD from seven independent experiments. ns: non-significant, *p < 0.05, **p < 0.01, ***p < 0.001 (Student's t test).

Self-interactions of both SAM and KH domains contribute to Bicc1 condensation *in vivo*

KH domains may contribute to Bicc1 condensation by interacting with Bicc1 itself. To evaluate this hypothesis, we first tested if HA-Bicc1 in HEK293T cell extracts binds to glutathione S-transferase (GST) fusion proteins of the entire KH repeat or of individual KH domains in pull-down assays (Figure 3A). Western blot analysis of bound proteins revealed that GST-KH and GST-KH_1 pulled down full-length and ΔSAM mutant HA-Bicc1, but only minimal amounts of HA-Bicc1 ΔKH. In contrast, the pull-down of HA-Bicc1 by KH_2 was close to the background of GST alone, and the KH_3 and the KHL 1 or 2 domains individually or combined remained insoluble. HA-Bicc1 and the ΔKH and ΔSAM truncation constructs also bound only weakly to a GST fusion of Bicc1 IVS. These results show that besides the known SAM:SAM interaction, a novel interface between KH domains significantly contributes to Bicc1 self-polymerization. To test whether the KH repeat cooperates with the SAM domain to condensate Bicc1 *in vivo*, we compared the co-polymerization of KH and/or SAM domain-mutant HA-Bicc1 with wild-type GFP-Bicc1 in HeLa and HEK293T cells where endogenous BICC1 protein levels are below detection by anti-Bicc1 immunostaining (Figure S4A). In addition, we chose HeLa cells because their firm adhesion, large cytoplasm, and high transfection efficiency also facilitate live imaging. As expected, HA-Bicc1 and GFP-Bicc1 perfectly colocalized in the same granules, confirming that HA and GFP tags do not perturb Bicc1 polymerization (Figure S4B). Importantly, co-localization with GFP-Bicc1 granules persisted even if HA-Bicc1 lacked the KH domains (ΔKH) or if its
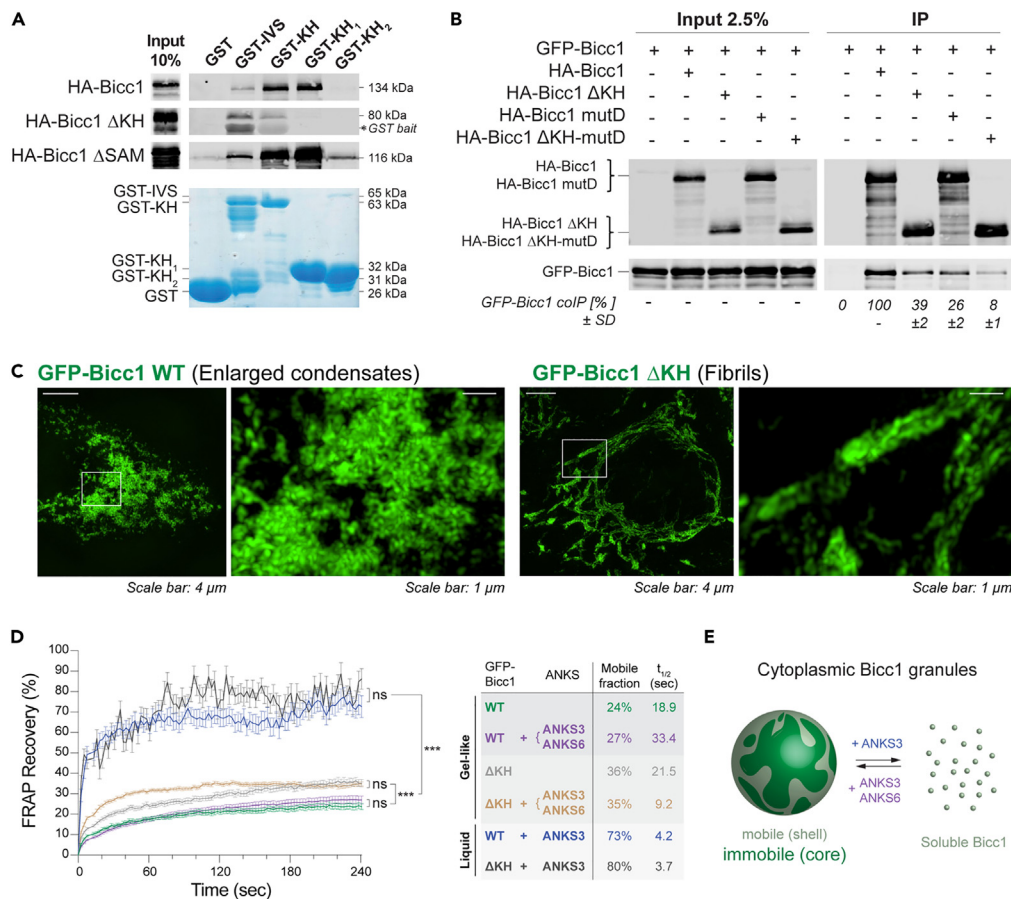
Figure 3. KH domains self-interact *in vitro* and contribute to the condensation of Bicc1 in gel-like granules *in vivo*

(A) Pull-down of HA-Bicc1 WT, ΔKH, and ΔSAM from HEK293T cell extracts by glutathione Sepharose beads coated with recombinant domains of Bicc1 fused to GST.

(B) Co-immunoprecipitation of GFP-Bicc1 with HA-Bicc1 WT, ΔKH, mutD, or ΔKH-mutD from HEK293T cell lysates. The amount of co-immunoprecipitated GFP-Bicc1 normalized to input is expressed relative to the HA-Bicc1 WT condition. The means ± SD of two experiments shown below the gel represent the ratio of co-immunoprecipitated GFP-Bicc1 to the input, normalized to the condition with HA-Bicc1 WT.

(C) Representative 3D SIM images of the categories "enlarged condensates" for GFP-Bicc1 WT and "fibrils" for the GFP-Bicc1 ΔKH mutant in transiently transfected HeLa cells.

(D) Fluorescence Recovery After Photo bleaching (FRAP) of GFP-Bicc1 WT and ΔKH granules in HeLa cells. ANKS3 with or without ANKS6 was co-transfected where indicated. Results are mean values from 34 individual measurements. Error bars show SEM. ns: non-significant, *p < 0.05, **p < 0.01, ***p < 0.001 (Student's *t* test).

(E) Schematic representation of the proposed relationship between the heterogeneous intragranular dynamics and the observed 3D SIM structure of GFP-Bicc1 granules, and their regulation by ANKS3 with or without ANKS6.

SAM:SAM interface was disrupted (mutD), but not if both mutations were combined (HA-Bicc1 ΔKH-mutD) (Figures S3 and S4B). Similarly, analysis in HEK293T cell extracts by co-immunoprecipitation revealed that the average binding of GFP-Bicc1 to HA-Bicc1 was reduced by only 61% with HA-Bicc1 ΔKH, or by 74% with HA-Bicc1 mutD, but by more than 92% with the double mutant (Figure 3B). These results unmask a hitherto unknown function of the KH repeats in promoting Bicc1 condensate formation by complementing the SAM domain-mediated self-interactions also *in vivo*.

KH domains modulate the interconnectivity of Bicc1 condensates

The interaction between Bicc1 KH domains implies that the valency of available interfaces is at least $v \geq 3$ (i.e., SAM^{EH}, SAM^{ML}, and KH) and therefore each Bicc1 molecule behaves as an interaction node where the network can potentially grow in three dimensions. To elucidate how the KH domains contribute to the expansion of Bicc1 condensates, we imaged GFP-Bicc1 and GFP-Bicc1 ΔKH at saturating expression levels

in HeLa cells that were transfected with a high dose of expression vector. After verifying that saturating expression levels in whole populations were comparable (Figure S4C), individual cells were imaged by confocal microscopy and binned into four categories based on the shape of the predominant condensates, including enlarged condensates (>3 μm^2), or regular granules ($\leq 3 \mu m^2$), granules with fibrillar connections, or fibrils (Figure S4D). Interestingly, wild-type GFP-Bicc1 (WT) always formed granules, and in 70% of the cells examined (n = 87/125), the saturating overexpression increased the granule sizes beyond 3 μm^2. In 30% of cells marked by at least 3-fold lower mean fluorescence intensity (n = 38/125), the sizes of GFP-Bicc1 granules remained below this threshold. In sharp contrast, GFP-Bicc1 ΔKH mainly formed only regular granules (n = 52/125 cells, 41.6%) or fibrillar structures (n = 28/125, 22.4%), or a combination of both (n = 42/125, 33.6%). Together, these results suggest that regular GFP-Bicc1 granules are interconnected in large condensates by KH domains, and not by the GFP tag. To validate this conclusion by higher resolution imaging, we used structured illumination microscopy (SIM). 3D reconstruction of enlarged GFP-Bicc1 WT condensates revealed that they all consisted of space-filling interconnected meshwork, whereas GFP-Bicc1 ΔKH polymers always extended longitudinally as fibrils (n $\geq$ 70 condensates per genotype from 12 cells each, Figure 3C). Besides confirming that Bicc1 polymers condensate independently of the RNA-binding KH domains, these data establish that KH domains favor the formation of granules and their interconnectivity at the expense of fibrils.

The interior of Bicc1 granules is inhomogeneous and contains a gel-like core

Multivalent interconnectivity within protein condensates tends to limit their exchange of molecules with the surrounding.[40,41] To evaluate the influence of KH domains on polymer dynamics, we compared GFP-Bicc1 WT and ΔKH condensates by fluorescence recovery after photobleaching (FRAP) analysis. We focused on the category "regular granules", where the sizes of GFP-Bicc1 WT and ΔKH condensates are comparable to endogenous Bicc1 in mouse kidneys and to each other (Figures 1B and S4E). Only 24% of GFP-Bicc1 fluorescence recovered after 4 min, highlighting the low molecular dynamics. By comparison, this mobile fraction was increased to 36% in the absence of the KH repeats, indicating that Bicc1 dynamics are limited at least in part by KH domains (Figure 3D, n = 34 granules per condition). However, the half-maximal fluorescence recovery was reached only after about 20 s for both constructs, indicating that KH domains reduce the mobile fraction of GFP without altering its diffusion rate. To test whether Bicc1 granule dynamics in addition are limited by the availability of ANKS3, we photobleached GFP-Bicc1 in cells that were co-transfected with ANKS3. Alternatively, and as an additional control to manipulate Bicc1 granule formation without changing other parameters, we co-transfected ANKS3 together with its specific antagonist ANKS6.[19] Whereas co-expression with ANKS3-Flag together with V5-ANKS6 did not significantly alter the gel-like GFP-Bicc1 dynamics, co-expression with ANKS3-Flag alone drastically increased the mobile fraction of GFP-Bicc1 and shortened the half-time of its fluorescence recovery to only 4 s, indicating that ANKS3 efficiently emulsified Bicc1 in the absence of ANKS6 but not in its presence (Figure 3D). Moreover, a comparison with GFP-Bicc1 ΔKH revealed that the gelation of GFP-Bicc1/ANKS3-Flag complexes by V5-ANKS6 was largely independent of RNA binding. Nevertheless, the half-time of fluorescence recovery of GFP-Bicc1 ΔKH in the joint presence of ANKS3-Flag and V5-ANKS6 decreased from 21 to 9 s. Thus, the KH domains are likely a hub of protein interactions also in the context of the heteromeric meshwork with ANKS3 and ANKS6. Taken together with the high-resolution imaging described above, our results suggest that GFP-Bicc1 granules consist of a mobile shell and an immobile "core". The core is reinforced by KH domains and needs protection from ANKS6 to resist emulsification and dissolution by ANKS3 (Figure 3E).

Live imaging reveals the dynamics of mRNA condensation by the Bicc1 protein scaffold in cytoplasmic granules

To distinguish whether Bicc1 induces phase transitioning of client transcripts or vice versa, we tagged their 3'UTRs with twelve MS2 hairpins and imaged their localization in real-time by labeling associated 2xMCP-Halo-NLS protein with the fluorescent Halo-tag ligand TMR.[42] In this system, a Halo-tagged tandem repeat of MS2 coat protein (MCP) is directed to the nucleus by a nuclear localization signal (NLS) but retained in the cytoplasm when tethered to MS2-tagged reporter mRNAs (Figure 4A). However, the original MS2 hairpin comprises a CGACGACG sequence.[43] Since this motif resembles the Bicc1 binding site GACGUGAC that we subsequently identified in the *Dand5* 3'UTR,[25] we decided to remove all bipartite GAC motifs to ensure that they cannot artificially bias competition among alternative targets or against potential inhibitors of RNA binding in favor of the reporter. As expected, luciferase control mRNA (Luc-12xMS2) localized diffusely throughout the cytoplasm in all cells examined, regardless of whether it was co-expressed with GFP-Bicc1 or with control GFP (Figure 4B). By contrast, GFP-Bicc1-12xMS2 mRNA
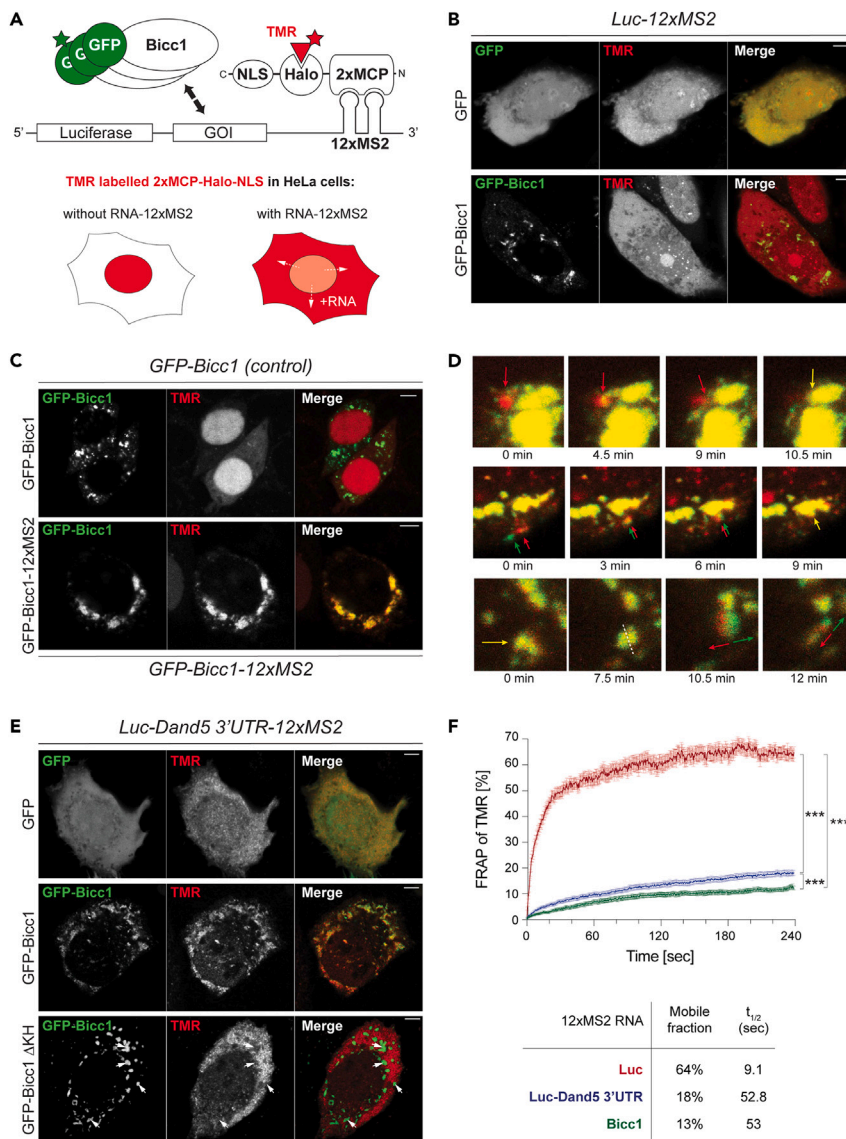
Figure 4. Bicc1 promotes the liquid-to-gel phase transition of target mRNAs

(A) Methodology to image the distribution of 12xMS2-tagged reporter mRNAs and its regulation by GFP-Bicc1. Halo-tagged MS2-coat protein (MCP) fused to a nuclear localization signal (NLS) normally accumulates in the nucleus, but when bound to a tandem repeat of 12 MS2 hairpins in reporter mRNAs of genes of interest (GOI), MCP fusion protein is also retained in the cytoplasm. HaloTag is labeled using the fluorescent ligand TMR.

(B and C) Live imaging of GFP or GFP-Bicc1 fluorescence (green), together with HaloTag/TMR-labeled (red) *Luc-12xMS2* control (B) or *GFP-Bicc1-12xMS2* (C) reporter mRNAs. Note that while TMR fluorescence was comparable in all nuclei, exposure times were adjusted to avoid saturation in cells where it is concentrated in Bicc1 granules. n ≥ 6 cells/condition. Scale bars, 5 μm.

(D) Time-lapse imaging of mRNA foci and GFP-Bicc1 granules undergoing fusion (top and mid lanes) or scission (bottom lane).

(E) Live imaging of GFP or GFP-Bicc1 WT or ΔKH fluorescence (green), together with HaloTag/TMR-labeled *Luc-Dand5 3'UTR-12xMS2* reporter mRNA (red). n = 12 cells/condition. Scale bars, 5 μm.

(F) Fluorescence Recovery After Photo bleaching (FRAP) of the *Luc-Dand5 3'UTR*-12xMS2 and GFP-Bicc1-12xMS2 transcripts enriched in the GFP-Bicc1 granules and marked by TMR bound to 2xMCP-Halo protein in HeLa cells. Luc-12xMS2 was a negative control. Results are mean values from 48 individual measurements. Error bars show SEM. ns: non-significant, *p < 0.05, **p < 0.01, ***p < 0.001 (Student's *t* test).

accumulated in GFP-Bicc1 granules (Figure 4C). Moreover, treatment with puromycin which releases nascent polypeptides from their ribosome-bound transcripts neither dispersed GFP-Bicc1 protein nor its mRNA (Figure S5A). Besides confirming that Bicc1 binds to its own transcripts,[13,23] these data indicate that the Bicc1 protein scaffold induces mRNA phase separation and that it does so independently of ongoing translation.

Interestingly, time-lapse movies revealed directional movements of GFP-Bicc1 condensates reminiscent of those in IMCD3 cells, and that GFP-Bicc1 particles undergoing fusion and fission also contained mRNA (Figures 4D, S5B, Videos S1, and S2). Alternatively, small GFP-Bicc1 RNP condensates in rare instances were seen dissociating from co-labeled mRNA. By contrast, enlarged Bicc1 RNP condensates were stationary, but continued to fuse with mobile Bicc1-free mRNA particles passing in their vicinity (Figure 4D, Videos S3, S4, and S5). These results suggest that Bicc1 can guide its own transcripts to cytoplasmic RNP granules in a process that becomes irreversible after small condensates are immobilized in stationary meshworks.

Bicc1 granules confer gel-like behavior to client mRNA bound to KH domains

To validate if Bicc1 imparts similar gel-like behavior to specific client mRNAs other than its own transcripts, we compared the influence of full-length GFP-Bicc1 and RNA binding-deficient Bicc1 ΔKH on the localization of Luc-*Dand5 3'UTR*-12xMS2. TMR labeling revealed that all cells expressing GFP-Bicc1 invariably concentrate Luc-*Dand5 3'UTR*-12xMS2 in cytoplasmic GFP-Bicc1 foci. By contrast, control cells expressing either GFP-Bicc1 ΔKH or GFP alone accumulated the reporter mRNA diffusely throughout the cytoplasm (Figure 4E). To assess the potential of Bicc1 granules to exchange mRNAs with their surrounding, we performed a FRAP analysis of the TMR signal. In cells expressing Luc-12xMS2 control mRNA, 64% of the cytoplasmic TMR fluorescence rapidly recovered, with a half-time of 9.1 s. By contrast, Dand5-3'UTR or GFP-Bicc1 mRNAs reduced the mobile fraction of associated TMR in GFP-Bicc1 granules to only 18% and 13%, respectively, and it slowed the half-time of TMR fluorescence recovery to 53 s (Figure 4F, n = 48 granules per condition). These data indicate that Bicc1 condensation immobilizes associated transcripts in gel-like granules where cargo only minimally diffuses in and out.[44]

ANKS3 and ANKS6 spatiotemporally couple RNA binding to Bicc1 phase transitioning

To assess whether the gel-like behavior of Bicc1 client mRNAs is regulated by protein-protein interactions with ANKS3, we imaged GFP-Bicc1-12xMS2 mRNA and GFP-Bicc1 protein in HeLa cells expressing ANKS3-Flag alone or together with V5-ANKS6. Control stainings after fixation validated that large GFP-Bicc1 condensates were dispersed specifically in cells that express ANKS3-Flag alone, but not in cells that co-express ANKS3-Flag together with V5-ANKS6 (Figure S6A), as described previously.[19] In good agreement, live imaging in cells without ANKS3-Flag revealed that GFP-Bicc1 and its TMR-labeled mRNA stably co-localize in large granules during at least 9 min (Figure 5A and Video S6). By contrast, co-transfection of ANKS3-Flag dispersed large GFP-Bicc1 granules and separated the residual small foci from the mRNA, as demonstrated by a strong anti-correlation of the peaks of GFP and TMR fluorescence (Figures 5B, S6B, and Video S7). Conversely, co-transfected ANKS6 restored the stable co-localization of GFP-Bicc1 mRNA with large GFP-Bicc1 condensates (Figures 5C, S6B, and Video S8). Importantly, co-recruitment of V5-ANKS6 also rescued large condensates of ANKS3-Flag with HA-Bicc1 ΔKH that cannot bind RNA (Figure S6A). Of note, ANKS3-Flag and V5-ANKS6 regulated the dispersal of GFP-Bicc1 granules even if transfected sequentially, demonstrating that nascent and pre-existing Bicc1 condensates respond similarly to these interacting factors (Figures S6C and S6D). These results show that the condensation of Bicc1 RNPs is a reversible process that can either be inhibited or stimulated by ANKS3 depending on ANKS6 and independently of KH domain binding to client mRNAs.

Truncated ANKS3 lacking the ankyrin repeat converts Bicc1 granules into spheroids devoid of reporter mRNA

Since changes in the valency or in binding affinities of client proteins can dramatically alter the architecture and dynamics of multivalent scaffolds,[40] we wondered how specific interfaces with ANKS3 other than SAM-SAM interactions may influence Bicc1 condensation. To address this, we imaged HA-Bicc1 granules in HeLa cells expressing truncated ANKS3-Flag lacking the ankyrin repeat (ANKS3 ΔNter) or the C-terminal coiled coil (ANKS3 ΔCter) (Figure S3). As shown previously, Bicc1 and ANKS3 ΔCter co-localize in cytoplasmic granules similar to those observed in the absence of ANKS3[19] (Figure S7). By contrast, ANKS3 ΔNter remodeled both GFP-Bicc1 and HA-Bicc1 granules into spherical condensates, as shown by an increase of the circularity coefficient from 0.294 ± 0.097 to 0.824 ± 0.111 (Figures 5D and S7, n = 30 granules per
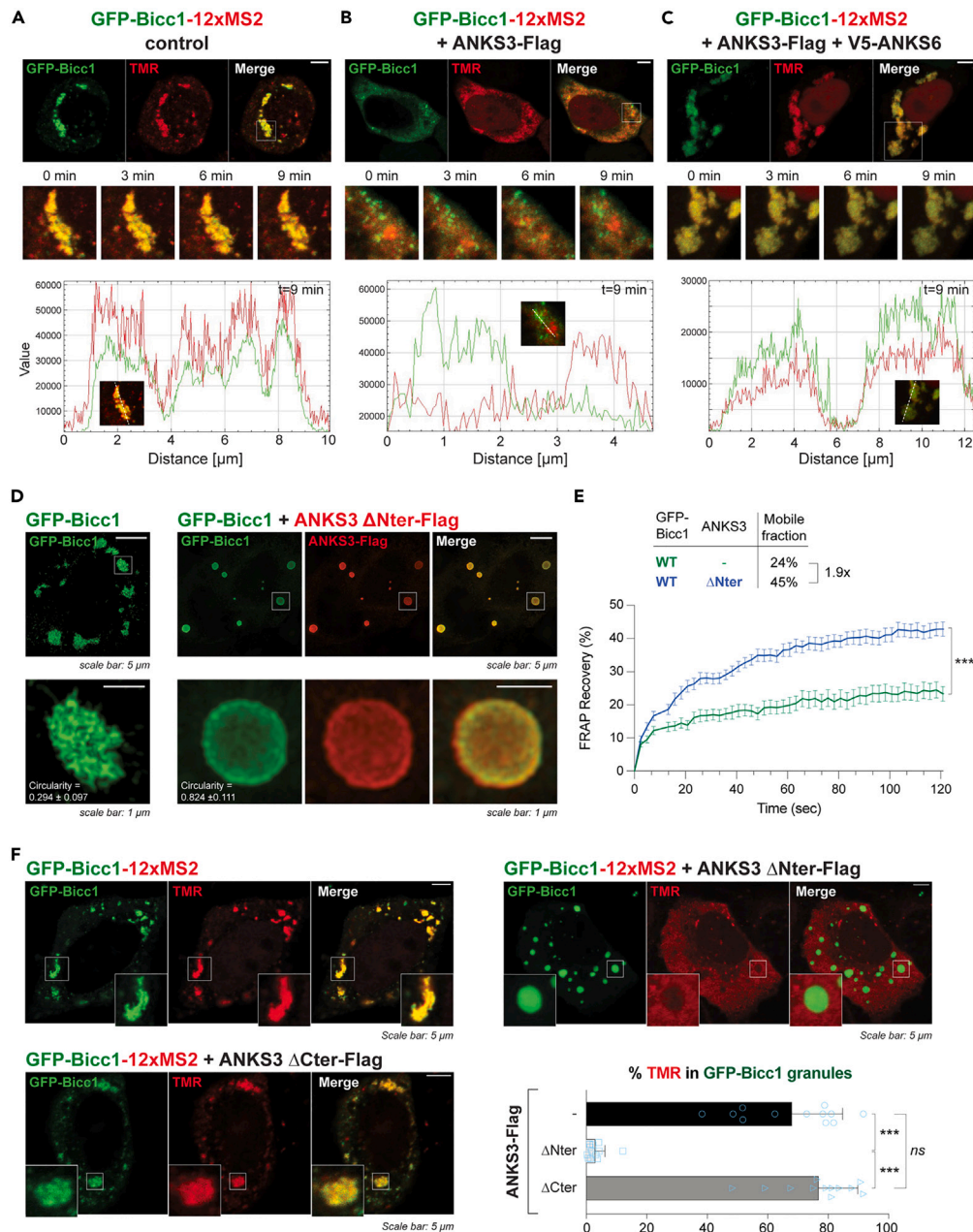
Figure 5. ANKS3 and ANKS6 synchronize Bicc1 phase separation and RNA binding

(A–C) Live imaging of GFP-Bicc1 (green) and its 12xMS2-tagged mRNA (red) in HeLa cells. GFP-Bicc1-12xMS2 was expressed alone (A), or in combination with ANKS3-Flag (B), or ANKS3-Flag and V5-ANKS6 (C). The fluorescent signal plots were generated using the multichannel plot profile analysis in ImageJ. Scale bars, 5 μm.

(D) 3D SIM images of GFP-Bicc1 and ANKS3 ΔNter-Flag co-transfected in HeLa cells. High magnifications of individual granules are shown at the bottom. Circularity coefficients ± SD were calculated using the ImageJ software from 30 individual granules per condition (a value of 1.0 indicates a perfect circle).

(E) Fluorescence Recovery After Photo bleaching (FRAP) of GFP-Bicc1 granules in HeLa cells with or without ANKS3 ΔNter-Flag co-transfection. Results are mean values from 22 individual measurements. Error bars show SEM. ns: non-significant, *p < 0.05, **p < 0.01, ***p < 0.001 (Student's t test).

(F) Live imaging of GFP-Bicc1 (green) and its *12xMS2-tagged* mRNA (red) in HeLa cells expressing or not ANKS3 ΔNter-Flag or ANKS3 ΔCter-Flag. The graph represents the percentage of TMR signal in GFP-Bicc1 granules calculated using the JACOP plugin in ImageJ. Data are means +SD from 12 individual cells. ns: non-significant, *p < 0.05, **p < 0.01, ***p < 0.001 (Student's t test).

condition). Correlating with this altered shape, physical contact among such condensates invariably led to their fusion into new spheroids, suggesting increased fluidity (Videos S9 and 10). In good agreement, FRAP analysis revealed that under these conditions, the mobile fraction of GFP-Bicc1 sharply increased from 24% to 45% (Figure 5E, n = 22 granules per condition), indicating liquid instead of gel-like behavior. We, therefore, wondered whether tuning the phase separation of Bicc1 by using modified versions of ANKS3 may also affect the condensation of target transcripts. To address this question, we imaged the effects of ANKS3 ΔNter and ΔCter on GFP-Bicc1 in real-time together with its 12xMS2-tagged mRNA. GFP-Bicc1 concentrated most of its mRNA in cytoplasmic granules even in the presence of ANKS3 ΔCter. By contrast, the GFP-Bicc1 spheroids induced by ANKS3 ΔNter were devoid of detectable TMR staining (Figure 5F and Video S11). These data show that the inhibitory effects of ANKS3 on RNA binding and on Bicc1 condensation can be uncoupled from each other: Whereas ANKS3 depends on both its Nter and Cter domains to disperse Bicc1 granules, only the C-terminal coiled coil directly participates in the inhibition of RNA binding.

DISCUSSION

Aberrant phase transitioning of proteins or mRNAs in a growing number of diseases highlights the urgent need to uncover the diversity of the biological mechanisms regulating this fundamental process *in vivo*. Here, high-resolution microscopy, live imaging, and biochemical analysis revealed that multiple self-interaction interfaces among protein domains rather than mRNA binding reversibly drive Bicc1 phase transitioning *in vitro* and *in vivo*. The resulting protein scaffolds showed actomyosin-dependent mobility, grew in size with increasing Bicc1 concentration, and controlled the localization and dynamics of target mRNAs in gel-like cytoplasmic granules. Furthermore, under the conditions examined, both Bicc1 granule formation and the immobilization of its client mRNAs were potently inhibited by ANKS3. Re-arrangement of the multivalent Bicc1/ANKS3 interactions in heterooligomers with co-recruited ANKS6 restored Bicc1 RNP condensation in gel-like granules. By contrast, deletion of the structured N-terminal domain of ANKS3 only rescued Bicc1 condensates but not their gel-like hardening or the co-condensation of mRNA, demonstrating that phase transitioning of Bicc1 can be uncoupled from mRNA binding to this protein scaffold. To our knowledge, such a dual control of RNP condensation by regulatory proteins represents a new mode of biological regulation of phase separation.

The KH domains as a new hub for Bicc1 self-interaction

The assembly of biomolecular condensates relies on IDRs containing multiple weak interaction motifs and/or on structured domains, which often exhibit RNA binding properties. RNA itself can also contribute to the phase separation by expanding the interaction network via protein:RNA and RNA:RNA interactions.[1] By contrast, the Bicc1 granules are primarily scaffolded by the orderly polymerization of its SAM domain. Consequently, deletion of the SAM domain, its aberrant elongation by a frame-shifting splice mutation in Bicc1[bpk/bpk] mice, or mutagenesis of its self-polymerization interface each prevent the condensation of Bicc1 *in vivo*.[9,10] The present work revealed that the KH repeat contributed nonetheless to Bicc1 condensation, both during *in vitro* sedimentation and when recruiting Bicc1 ΔSAM into cytoplasmic GFP-Bicc1 co-polymers. Binding to RNA was not responsible, as shown by the sedimentation of Bicc1 regardless of the presence of a synthetic target RNA or treatment with RNase A. Instead, we discovered that the KH domains self-interact, at least through their KH1, consistent with the dimeric structure of human BICC1 KH1 determined by X-ray crystallography (PDB: 6GY4). Elevating the salt concentration sufficed to dissolve Bicc1 sediments. This salt-in effect strongly suggests a role for stereospecific electrostatic contacts such as the hydrogen bonds between two Bicc1 KH1 domains. By contrast, in protein condensates induced by non-ionic interactions of disordered regions, high salt typically favors re-entrant phase transitions or aggregation.[45] Moreover, as little as 150 mM NaCl led to a 3-fold decrease in KH domain-mediated Bicc1 sedimentation. The inhibition by a physiological salt concentration may explain why the nucleation of Bicc1 condensates *in vivo* depends on the SAM domain. To our knowledge, the finding that KH domains contribute to condensation through protein-protein interactions and thereby regulate the de-mixing of associated transcripts has not been reported previously.

Bicc1 KH and SAM domains cooperate to assemble a 3D meshwork with gel-like properties

The identification of an additional self-interaction interface has several implications for the function of Bicc1. Foremost, while ML and EH surfaces link the SAM domains to each other,[19] the KH domains increase the valency of known self-interactions by providing at least one additional docking site for yet another Bicc1

monomer, or to crosslink oligomers to each other. The measurement of protein dynamics by FRAP revealed that the majority of GFP-Bicc1 protein inside granules forms an immobile core that is gel-like, as defined by the lack of exchange of molecules with the surrounding liquid. Only a minority fraction of 24% was mobile. Its exchange rate ($t_{1/2} \simeq 20$ s) is reminiscent of SGs and PBs that form by liquid-liquid phase transitioning.[46–48] Deletion of the KH repeat increased this mobile fraction 1.5-fold. As the stability of condensates generally correlates with the connectivity of their components,[40,41] this result further supports a role for KH domains in cross-linking Bicc1 polymers nucleated by the SAM domain. In line with this interpretation, we found that the novel self-interaction mediated by KH domains modulates Bicc1 granule shapes. Thus, unlike the space-filling interconnected meshwork formed by full-length GFP-Bicc1, GFP-Bicc1 ΔKH polymers instead formed fibrillar structures. Previous analysis by cryoelectron microscopy established that rod-like fibrils can also be assembled in vitro by head-to-tail polymerization of isolated Bicc1 SAM domain alone.[49] Together, these observations suggest that the Bicc1 SAM domain nucleates longitudinally growing fibrils that are remodeled by KH domains into a meshwork of interconnected granules.

Co-condensation of client mRNAs with specific scaffold proteins is typically driven by IDRs. In sharp contrast, evidence for a similar role of the disordered IVS of Bicc1 is lacking. However, at least a passive role of the IVS in Bicc1 condensation should be considered since flexible linkers are known to influence protein gelation.[50] Comprising a relatively long sequence of 431 amino acids, the IVS may increase the conformational freedom of structured domains to expand the Bicc1 network and allow ANKS3 and ANKS6 to regulate access to client mRNAs. Additional layers of regulation of many protein condensates frequently include post-translational modifications (PTMs).[51] Tools introduced here to determine what governs Bicc1 RNP dynamics pave the way to investigate whether the Bicc1 IVS and its numerous annotated PTMs further modulate phase transitioning, e.g. through repulsion, rigidification, and/or by regulating the binding of specific interacting factors.

Bicc1 promotes the liquid-to-gel transitioning of client mRNAs

Our FRAP analysis of target mRNAs revealed that Bicc1 promotes liquid-to-gel transitions of its target mRNAs. Interestingly, the molecular diffusion of bound mRNAs decreased below that of GFP-Bicc1 protein itself, possibly reflecting the marked difference in size and gyration radius of mRNAs compared to proteins.[52] In addition, intermolecular RNA-RNA interactions or re-association with RNA-free KH domains may further restrain mRNA mobility inside the Bicc1 meshwork. In return, feedback from the client transcripts on granule dynamics is not excluded. Indeed, a 27xMS2-tagged Adcy6 3′UTR reporter mRNA has previously been shown to bind to Bicc1/ANKS3 complexes independently of ANKS6.[19] This 27xMS2 tag comprises 12 copies of the CGACGACG sequence that includes two GAC motifs akin to the Bicc1 binding site GACGUGAC in the Dand5 3′UTR.[25] By contrast, reporter mRNAs that we tagged with only 12 repeats of a different MS2 sequence devoid of artificial bipartite GAC motifs were effectively barred from entering Bicc1 granules by ANKS3 (Figure 4). This interesting example strongly suggests that ANKS3 hinders access of Bicc1 to mRNA by direct competitive inhibition, rather than indirectly through its inhibitory effect on Bicc1 phase transitioning. In line with this interpretation, deletion of the structured N-terminal domain of ANKS3 rescued Bicc1 condensates, but not their gel-like hardening or the co-condensation of mRNA. These observations confirm that phase transitioning of Bicc1 and mRNA binding can be uncoupled and hence are not causally linked, even though both of these processes happen to be co-regulated by ANKS3 and ANKS6.

ANKS3 and ANKS6 alter the properties of the Bicc1 meshwork and modulate the retention of client mRNAs

Previously, we have shown that ANKS3 acts as a negative regulator of Bicc1 granule formation by hindering SAM polymerization through its Cter domain (Rothé et al., 2018). Here, we observed that removing the Nter domain of ANKS3 prevents Bicc1 granule dissolution and reshapes the complexes into spherical condensates. The shape of a condensate is governed by the surface tension, a mechanical force at the boundary between the dense phase and surrounding liquid.[53] Liquid condensates naturally tend to adopt a spherical shape to minimize their interface with the solvent. Our observation that ANKS3 ΔNter colocalizes with Bicc1 in spheres suggests that the Nter domain of ANKS3 contributes to the emulsification of the Bicc1 granules by altering the surface tension. Hence, the dispersal of Bicc1 by ANKS3 seems to rely on the steric hindrance of SAM polymerization by its Cter domain[19] and on the modulation of the surface tension by its Nter domain, the combination of both forces being required to dissolve Bicc1 granules. By contrast, the co-recruitment of ANKS6 to Bicc1-ANKS3 complexes rescues both the assembly and the phase separation

of Bicc1 RNPs. Together, these findings suggest that ANKS3 and ANKS6 synchronize and spatially couple specific RNA binding of Bicc1 with its phase separation.

Actomyosin-dependent mobility of the Bicc1 granules suggests a role in RNA transport

Our live imaging experiments revealed that GFP-Bicc1 granules are mobile, with a subset showing directional movements driven by actomyosin and to a lesser extent by microtubules. In line with this observation, previous analysis of the Bicc1 protein interactome identified components of the actomyosin network, including filamin, alpha-actinin-4, actin-like protein 6A, and several ARHGEF and ARHGAP proteins.[15] By contrast, PBs use microtubules for long-range movements and remain stationary when associated with actin.[54] Spikes of directional motion of small GFP-Bicc1 granules and associated RNA coincided with fusion and fission, or with their incorporation into larger stationary Bicc1 RNPs. In neurons, localization of RNA in granules allows to coordinate their translation in space and time.[55] These observations warrant further study to assess whether Bicc1 granules organize the transport of a subset of transcripts along the cytoskeleton to control their translation at specific subcellular locations, such as the centrosome.[16]

Given the large number of Bicc1-interacting factors, ANKS3 and ANKS6 are unlikely the only factors that influence the solubility of Bicc1 and its RNP dynamics. However, our present findings are consistent with known *Anks6* and *Anks3* functions *in vivo*. Cystic kidneys of *Anks6*[cy/+] rats accumulate calcium oxalate crystals, possibly due to impaired urine flow sensing, suggesting the implication of *Anks6* in a program of reversible renal tubule dilation that allows urine flow to flush out crystals during adult tissue homeostasis.[56,57] An attractive hypothesis is that ANKS6 may relieve Bicc1 from its inhibition by ANKS3 in metronomic quantities determined by flow stimulation of primary cilia in order to regulate tubule dilatation via the reversible repression of specific transcripts such as AC6. Therefore, future studies should address whether such a program relies on Bicc1 condensates and whether disruption of their dynamics is responsible for cyst formation and other ciliopathy defects.

Limitations of the study

Studying protein dynamics requires fluorescent fusion proteins. As fusion of GFP to the Bicc1 C-terminus inhibits Bicc1 function and interferes with head-to-tail polymerization of the SAM domain, we had to fuse GFP to the N-terminus. Importantly, GFP slightly increased Bicc1 solubility in cell extracts rather than reducing it, and it did not alter Bicc1 function in any of the cell-based assays examined. Nevertheless, we cannot formally rule out the possibility that GFP could potentially skew some protein interactions of the adjacent KH domains. A related limitation is that the behavior of the Bicc1 protein network and the influence of specific protein domain deletions employed here should be expected to be malleable by endogenous Bicc1 or its partner proteins. Therefore, we validated all of our conclusions by comparing Bicc1 with and without GFP in human HeLa and HEK293T cells that express only trace amounts of BICC1 mRNA, and in CRISPR-edited IMCD3 cells, where exon 1 of endogenous *Bicc1* was disrupted by a frame-shifting indel mutation. Finally, among the commercially available antibodies, none were specific for ANKS3, and specific anti-ANKS6 antibodies are all from rabbits, precluding to conduct co-immunostaining of endogenous ANKS3 or ANKS6 together with rabbit anti-Bicc1 antibodies, and hence to determine when and where exactly the observed interactions with Bicc1 RNPs occur during embryonic development or in kidneys.

STAR★METHODS

Detailed methods are provided in the online version of this paper and include the following:

- KEY RESOURCES TABLE
- RESOURCE AVAILABILITY
  - Lead contact
  - Materials availability
  - Data and code availability
- EXPERIMENTAL MODEL
- METHOD DETAILS
  - Antibodies
  - Plasmids
  - Plasmid transfection and cell treatment
  - Purification of GST fusion proteins
  - Sedimentation of membraneless compartments by stepwise differential centrifugation

  ○ Protein co-immunoprecipitation assay in HEK293T cells
  ○ Reconstitution of multiprotein complexes and RNP by GST pull-down
  ○ Tracking of GFP Bicc1 granules
  ○ Classification of GFP-Bicc1 condensates by their shapes, and quantification of mRNA co-localization
  ○ FRAP analysis
  ○ Structured illumination microscopy
  ○ Immunofluorescence staining
  ○ Protein-RNA colocalization by time-lapse imaging
● QUANTIFICATION AND STATISTICAL ANALYSIS

SUPPLEMENTAL INFORMATION

Supplemental information can be found online at https://doi.org/10.1016/j.isci.2023.106855.

AUTHOR CONTRIBUTIONS

Conceptualization and Methodology, B.R., S.F., C.G., and D.B.C.; Validation, B.R. and D.B.C.; Formal analysis and Investigation, B.R., S.F., C.G., and C.S.; Data Curation, B.R.; Writing – Original Draft, B.R. and D.B.C.; Writing – Review & Editing, B.R., S.F., and D.B.C.; Visualization, B.R.; Supervision, D.B.C.; Project Administration, D.B.C.; Funding Acquisition, S.F. and D.B.C.

DECLARATION OF INTERESTS

The authors declare no competing interests.

INCLUSION AND DIVERSITY

We support inclusive, diverse, and equitable conduct of research.

REFERENCES

1. Boeynaems, S., Alberti, S., Fawzi, N.L., Mittag, T., Polymenidou, M., Rousseau, F., Schymkowitz, J., Shorter, J., Wolozin, B., Van Den Bosch, L., et al. (2018). Protein phase separation: a new phase in cell biology. Trends Cell Biol. *28*, 420–435. https://doi.org/10.1016/j.tcb.2018.02.004.

2. Riggs, C.L., Kedersha, N., Ivanov, P., and Anderson, P. (2020). Mammalian stress granules and P bodies at a glance. J. Cell Sci. *133*, jcs242487. https://doi.org/10.1242/jcs.242487.

3. Dignon, G.L., Best, R.B., and Mittal, J. (2020). Biomolecular phase separation: from molecular driving forces to macroscopic properties. Annu. Rev. Phys. Chem. *71*, 53–75. https://doi.org/10.1146/annurev-physchem-071819-113553.

4. Van Treeck, B., and Parker, R. (2018). Emerging roles for intermolecular RNA-RNA interactions in RNP assemblies. Cell *174*, 791–802. https://doi.org/10.1016/j.cell.2018.07.023.

5. Wang, B., Zhang, L., Dai, T., Qin, Z., Lu, H., Zhang, L., and Zhou, F. (2021). Liquid–liquid phase separation in human health and diseases. Signal Transduct. Target. Ther. *6*, 290. https://doi.org/10.1038/s41392-021-00678-1.

6. Hubstenberger, A., Courel, M., Bénard, M., Souquere, S., Ernoult-Lange, M., Chouaib, R., Yi, Z., Morlot, J.B., Munier, A., Fradet, M., et al. (2017). P-body purification reveals the condensation of repressed mRNA regulons. Mol. Cell *68*, 144–157.e5. https://doi.org/10.1016/j.molcel.2017.09.003.

7. Youn, J.Y., Dyakov, B.J.A., Zhang, J., Knight, J.D.R., Vernon, R.M., Forman-Kay, J.D., and Gingras, A.C. (2019). Properties of stress granule and P-body proteomes. Mol. Cell *76*, 286–294. https://doi.org/10.1016/j.molcel.2019.09.014.

8. Estrada Mallarino, L., Engel, C., Ilık, İ.A., Maticzka, D., Heyl, F., Müller, B., Yakulov, T.A., Dengjel, J., Backofen, R., Akhtar, A., and Walz, G. (2020). Nephronophthisis gene products display RNA-binding properties and are recruited to stress granules. Sci. Rep. *10*, 15954. https://doi.org/10.1038/s41598-020-72905-8.

9. Maisonneuve, C., Guilleret, I., Vick, P., Weber, T., Andre, P., Beyer, T., Blum, M., and Constam, D.B. (2009). Bicaudal C, a novel regulator of Dvl signaling abutting

RNA-processing bodies, controls cilia orientation and leftward flow. Development *136*, 3019–3030. https://doi.org/10.1242/dev.038174.

10. Rothé, B., Leal-Esteban, L., Bernet, F., Urfer, S., Doerr, N., Weimbs, T., Iwaszkiewicz, J., and Constam, D.B. (2015). Bicc1 polymerization regulates the localization and silencing of bound mRNA. Mol. Cell Biol. *35*, 3339–3353. https://doi.org/10.1128/mcb.00341-15.

11. Tran, U., Zakin, L., Schweickert, A., Agrawal, R., Döger, R., Blum, M., De Robertis, E.M., and Wessely, O. (2010). The RNA-binding protein bicaudal C in the kidney by antagonizing miR-17 activity. Development *137*, 1107–1116. https://doi.org/10.1242/dev.046045.

12. Youn, J.Y., Dunham, W.H., Hong, S.J., Knight, J.D.R., Bashkurov, M., Chen, G.I., Bagci, H., Rathod, B., MacLeod, G., Eng, S.W.M., et al. (2018). High-density proximity mapping reveals the subcellular organization of mRNA-associated granules and bodies. Mol. Cell *69*, 517–532.e11. https://doi.org/10.1016/j.molcel.2017.12.020.

13. Chicoine, J., Benoit, P., Gamberi, C., Paliouras, M., Simonelig, M., and Lasko, P. (2007). Bicaudal-C recruits CCR4-NOT deadenylase to target mRNAs and regulates oogenesis, cytoskeletal organization, and its own expression. Dev. Cell *13*, 691–704. https://doi.org/10.1016/j.devcel.2007.10.002.

14. Kugler, J.-M., Chicoine, J., and Lasko, P. (2009). Bicaudal-C associates with a Trailer Hitch/Me31B complex and is required for efficient Gurken secretion. Dev. Biol. *328*, 160–172. https://doi.org/10.1016/j.ydbio.2009.01.024.

15. Leal-Esteban, L.C., Rothé, B., Fortier, S., Isenschmid, M., and Constam, D.B. (2018). Role of Bicaudal C1 in renal gluconeogenesis and its novel interaction with the CTLH complex. PLoS Genet. *14*, e1007487. https://doi.org/10.1371/journal.pgen.1007487.

16. Iaconis, D., Monti, M., Renda, M., van Koppen, A., Tammaro, R., Chiaravalli, M., Cozzolino, F., Pignata, P., Crina, C., Pucci, P., et al. (2017). The centrosomal OFD1 protein interacts with the translation machinery and regulates the synthesis of specific targets. Sci. Rep. *7*, 1224. https://doi.org/10.1038/s41598-017-01156-x.

17. Kim, C.A., Phillips, M.L., Kim, W., Gingery, M., Tran, H.H., Robinson, M.A., Faham, S., and Bowie, J.U. (2001). Polymerization of the SAM domain of TEL in leukemogenesis and transcriptional repression. EMBO J. *20*, 4173–4182. https://doi.org/10.1093/emboj/20.15.4173.

18. Bienz, M. (2020). Head-to-tail polymerization in the assembly of biomolecular condensates. Cell *182*, 799–811. https://doi.org/10.1016/j.cell.2020.07.037.

19. Rothé, B., Leettola, C.N., Leal-Esteban, L., Cascio, D., Fortier, S., Isenschmid, M., Bowie, J.U., and Constam, D.B. (2018). Crystal structure of Bicc1 SAM polymer and mapping of interactions between the ciliopathy-associated proteins Bicc1, ANKS3, and ANKS6. Structure *26*, 209–224.e6. https://doi.org/10.1016/j.str.2017.12.002.

20. Cogswell, C., Price, S.J., Hou, X., Guay-Woodford, L.M., Flaherty, L., and Bryda, E.C. (2003). Positional cloning of jcpk/bpk locus of the mouse. Mamm. Genome *14*, 242–249. https://doi.org/10.1007/s00335-002-2241-0.

21. Wallace, D.P. (2011). Cyclic AMP-mediated cyst expansion. Biochim. Biophys. Acta *1812*, 1291–1300. https://doi.org/10.1016/j.bbadis.2010.11.005.

22. Rees, S., Kittikulsuth, W., Roos, K., Strait, K.A., Van Hoek, A., and Kohan, D.E. (2014). Adenylyl cyclase 6 deficiency ameliorates polycystic kidney disease. J. Am. Soc. Nephrol. *25*, 232–237. https://doi.org/10.1681/ASN.2013010077.

23. Piazzon, N., Maisonneuve, C., Guilleret, I., Rotman, S., and Constam, D.B. (2012). Bicc1 links the regulation of cAMP signaling in polycystic kidneys to microRNA-induced gene silencing. J. Mol. Cell Biol. *4*, 398–408. https://doi.org/10.1093/jmcb/mjs027.

24. Maerker, M., Getwan, M., Dowdle, M.E., McSheene, J.C., Gonzalez, V., Pelliccia, J.L., Hamilton, D.S., Yartseva, V., Vejnar, C., Tingler, M., et al. (2021). Bicc1 and Dicer regulate left-right patterning through post-transcriptional control of the Nodal inhibitor Dand5. Nat. Commun. *12*, 5482. https://doi.org/10.1038/s41467-021-25464-z.

25. Minegishi, K., Rothé, B., Komatsu, K.R., Ono, H., Ikawa, Y., Nishimura, H., Katoh, T.A., Kajikawa, E., Sai, X., Miyashita, E., et al. (2021). Fluid flow-induced left-right asymmetric decay of Dand5 mRNA in the mouse embryo requires a Bicc1-Ccr4 RNA degradation complex. Nat. Commun. *12*, 4071. https://doi.org/10.1038/s41467-021-24295-2.

26. Bakey, Z., Bihoreau, M.T., Piedagnel, R., Delestré, L., Arnould, C., De Villiers, A.D., Devuyst, O., Hoffmann, S., Ronco, P., Gauguier, D., and Lelongt, B. (2015). The SAM domain of ANKS6 has different interacting partners and mutations can induce different cystic phenotypes. Kidney Int. *88*, 299–310. https://doi.org/10.1038/ki.2015.122.

27. Nakajima, Y., Kiyonari, H., Mukumoto, Y., and Yokoyama, T. (2018). The Inv compartment of renal cilia is an intraciliary signal-activating center to phosphorylate ANKS6. Kidney Int. *93*, 1108–1117. https://doi.org/10.1016/j.kint.2017.11.016.

28. Stagner, E.E., Bouvrette, D.J., Cheng, J., and Bryda, E.C. (2009). The polycystic kidney disease-related proteins Bicc1 and SamCystin interact. Biochem. Biophys. Res. Commun. *383*, 16–21. https://doi.org/10.1016/j.bbrc.2009.03.113.

29. Yakulov, T.A., Yasunaga, T., Ramachandran, H., Engel, C., Müller, B., Hoff, S., Dengjel, J., Lienkamp, S.S., and Walz, G. (2015). Anks3 interacts with nephronophthisis proteins and is required for normal renal development. Kidney Int. *87*, 1191–1200. https://doi.org/10.1038/ki.2015.17.

30. Brown, J.H., Bihoreau, M.T., Hoffmann, S., Kränzlin, B., Tychinskaya, I., Obermüller, N., Podlich, D., Boehn, S.N., Kaisaki, P.J., Megel, N., et al. (2005). Missense mutation in sterile α motif of novel protein SamCystin is associated with polycystic kidney disease in (cy/+) rat. J. Am. Soc. Nephrol. *16*, 3517–3526. https://doi.org/10.1681/ASN.2005060601.

31. Czarnecki, P.G., Gabriel, G.C., Manning, D.K., Sergeev, M., Lemke, K., Klena, N.T., Liu, X., Chen, Y., Li, Y., San Agustin, J.T., et al. (2015). ANKS6 is the critical activator of NEK8 kinase in embryonic situs determination and organ patterning. Nat. Commun. *6*, 6023. https://doi.org/10.1038/ncomms7023.

32. Hoff, S., Halbritter, J., Epting, D., Frank, V., Nguyen, T.M.T., Van Reeuwijk, J., Boehlke, C., Schell, C., Yasunaga, T., Helmstädter, M., et al. (2013). ANKS6 is a central component of a nephronophthisis module linking NEK8 to INVS and NPHP3. Nat. Genet. *45*, 951–956. https://doi.org/10.1038/ng.2681.

33. Taskiran, E.Z., Korkmaz, E., Gucer, S., Kosukcu, C., Kaymaz, F., Koyunlar, C., Bryda, E.C., Chaki, M., Lu, D., Vadnagara, K., et al. (2014). Mutations in ANKS6 cause a nephronophthisis-like phenotype with ESRD. J. Am. Soc. Nephrol. *25*, 1653–1661. https://doi.org/10.1681/ASN.2013060646.

34. Shamseldin, H.E., Yakulov, T.A., Hashem, A., Walz, G., and Alkuraya, F.S. (2016). ANKS3 is mutated in a family with autosomal recessive laterality defect. Hum. Genet. *135*, 1233–1239. https://doi.org/10.1007/s00439-016-1712-4.

35. Rothé, B., Gagnieux, C., Leal-Esteban, L.C., and Constam, D.B. (2020). Role of the RNA-binding protein Bicaudal-C1 and interacting factors in cystic kidney diseases. Cell. Signal. *68*, 109499. https://doi.org/10.1016/j.cellsig.2019.109499.

36. Schlimpert, M., Lagies, S., Budnyk, V., Müller, B., Walz, G., and Kammerer, B. (2018). Metabolic phenotyping of Anks3 depletion in mIMCD-3 cells - a putative nephronophthisis candidate. Sci. Rep. *8*, 9022. https://doi.org/10.1038/s41598-018-27389-y.

37. Teixeira, D., Sheth, U., Valencia-Sanchez, M.A., Brengues, M., and Parker, R. (2005). Processing bodies require RNA for assembly and contain nontranslating mRNAs. RNA *11*, 371–382. https://doi.org/10.1261/rna.7258505.

38. Jain, S., Wheeler, J.R., Walters, R.W., Agrawal, A., Barsic, A., and Parker, R. (2016). ATPase-modulated stress granules contain a diverse proteome and substructure. Cell *164*, 487–498. https://doi.org/10.1016/j.cell.2015.12.038.

39. Namkoong, S., Ho, A., Woo, Y.M., Kwak, H., and Lee, J.H. (2018). Systematic characterization of stress-induced RNA granulation. Mol. Cell *70*, 175–187.e8. https://doi.org/10.1016/j.molcel.2018.02.025.

40. Sanchez-Burgos, I., Espinosa, J.R., Joseph, J.A., and Collepardo-Guevara, R. (2021). Valency and binding affinity variations can regulate the multilayered organization of protein condensates with many components.

Biomolecules *11*, 278. https://doi.org/10.3390/biom11020278.

41. Espinosa, J.R., Joseph, J.A., Sanchez-Burgos, I., Garaizar, A., Frenkel, D., and Collepardo-Guevara, R. (2020). Liquid network connectivity regulates the stability and composition of biomolecular condensates with many components. Proc. Natl. Acad. Sci. USA *117*, 13238–13247. https://doi.org/10.1073/pnas.1917569117.

42. Halstead, J.M., Lionnet, T., Wilbertz, J.H., Wippich, F., Ephrussi, A., Singer, R.H., and Chao, J.A. (2015). An RNA biosensor for imaging the first round of translation from single cells to living animals. Science *347*, 1367–1671. https://doi.org/10.1126/science.aaa3380.

43. Bertrand, E., Chartrand, P., Schaefer, M., Shenoy, S.M., Singer, R.H., and Long, R.M. (1998). Localization of ASH1 mRNA particles in living yeast. Mol. Cell *2*, 437–445. https://doi.org/10.1016/S1097-2765(00)80143-4.

44. Jain, A., and Vale, R.D. (2017). RNA phase transitions in repeat expansion disorders. Nature *546*, 243. https://doi.org/10.1038/nature22386.

45. Krainer, G., Welsh, T.J., Joseph, J.A., Espinosa, J.R., Wittmann, S., de Csilléry, E., Sridhar, A., Toprakcioglu, Z., Gudiškytė, G., Czekalska, M.A., et al. (2021). Reentrant liquid condensate phase of proteins is stabilized by hydrophobic and non-ionic interactions. Nat. Commun. *12*, 1085. https://doi.org/10.1038/s41467-021-21181-9.

46. Aizer, A., Kalo, A., Kafri, P., Shraga, A., Ben-Yishay, R., Jacob, A., Kinor, N., and Shav-Tal, Y. (2014). Quantifying mRNA targeting to P-bodies in living human cells reveals their dual role in mRNA decay and storage. J. Cell Sci. *127*, 4443–4456. https://doi.org/10.1242/jcs.152975.

47. Kedersha, N., Cho, M.R., Li, W., Yacono, P.W., Chen, S., Gilks, N., Golan, D.E., and Anderson, P. (2000). Dynamic shuttling of TIA-1 accompanies the recruitment of mRNA to mammalian stress granules. J. Cell Biol. *151*, 1257–1268. https://doi.org/10.1083/jcb.151.6.1257.

48. Kedersha, N., Stoecklin, G., Ayodele, M., Yacono, P., Lykke-Andersen, J., Fritzler, M.J., Scheuner, D., Kaufman, R.J., Golan, D.E., and Anderson, P. (2005). Stress granules and processing bodies are dynamically linked sites of mRNP remodeling. J. Cell Biol. *169*, 871–884. https://doi.org/10.1083/jcb.200502088.

49. Knight, M.J., Leettola, C., Gingery, M., Li, H., and Bowie, J.U. (2011). A human sterile alpha motif domain polymerizome. Protein Sci. *20*, 1697–1706. https://doi.org/10.1002/pro.703.

50. Harmon, T.S., Holehouse, A.S., Rosen, M.K., and Pappu, R.V. (2017). Intrinsically disordered linkers determine the interplay between phase separation and gelation in multivalent proteins. Elife *6*, e30294. https://doi.org/10.7554/eLife.30294.

51. Snead, W.T., and Gladfelter, A.S. (2019). The control centers of biomolecular phase separation: how membrane surfaces, PTMs, and active processes regulate condensation. Mol. Cell *76*, 295–305. https://doi.org/10.1016/j.molcel.2019.09.016.

52. Hyeon, C., Dima, R.I., and Thirumalai, D. (2006). Size, shape, and flexibility of RNA structures. J. Chem. Phys. *125*, 194905. https://doi.org/10.1063/1.2364190.

53. Hyman, A.A., Weber, C.A., and Jülicher, F. (2014). Liquid-liquid phase separation in biology. Annu. Rev. Cell Dev. Biol. *30*, 39–58. https://doi.org/10.1146/annurev-cellbio-100913-013325.

54. Koppers, M., Özkan, N., and Farías, G.G. (2020). Complex interactions between membrane-bound organelles, biomolecular condensates and the cytoskeleton. Front. Cell Dev. Biol. *8*, 618733. https://doi.org/10.3389/fcell.2020.618733.

55. Langdon, E.M., and Gladfelter, A.S. (2018). A new lens for RNA localization: liquid-liquid phase separation. Annu. Rev. Microbiol. *72*, 255–271. https://doi.org/10.1146/annurev-micro-090817-062814.

56. Torres, J.A., Rezaei, M., Broderick, C., Lin, L., Wang, X., Hoppe, B., Cowley, B.D., Savica, V., Torres, V.E., Khan, S., et al. (2019). Crystal deposition triggers tubule dilation that accelerates cystogenesis in polycystic kidney disease. J. Clin. Invest. *129*, 4506–4522. https://doi.org/10.1172/JCI128503.

57. Torres, J.A., Kruger, S.L., Broderick, C., Amarlkhagva, T., Agrawal, S., Dodam, J.R., Mrug, M., Lyons, L.A., and Weimbs, T. (2019). Ketosis ameliorates renal cyst growth in polycystic kidney disease. Cell Metab. *30*, 1007–1023.e5. https://doi.org/10.1016/j.cmet.2019.09.012.

STAR★METHODS

KEY RESOURCES TABLE

REAGENT or RESOURCE	SOURCE	IDENTIFIER
Antibodies		
Monoclonal anti-HA (produced in rabbit)	Sigma	Cat#H6908; RRID: AB_260070
Monoclonal anti-FLAG® M2 (produced in mouse)	Sigma	Cat#F3165; RRID: AB_259529
Monoclonal mouse anti-γTubulin	Sigma	Cat#T6557; RRID: AB_477584
Polyclonal anti-ANKS6 (produced in rabbit)	Sigma	Cat#HPA008355; RRID: AB_2058277
Polyclonal rabbit anti-GAPDH	Abcam	Cat#ab70699; RRID: AB_1209569
Monoclonal anti-HA−Agarose antibody (produced in mouse)	Sigma	Cat#A2095; AB_257974
IRDye® 680RD Donkey anti-Mouse IgG Secondary Antibody	LI-COR Biosciences	Cat# 926-68072; RRID: AB_2814912
IRDye® 800CW Donkey anti-Rabbit IgG Secondary Antibody	LI-COR Biosciences	Cat# 926-32213; RRID: AB_2715510
Bacterial and Virus Strains		
BL21(DE3) Chemically Competent *E. coli*	Invitrogen	Cat#C600003
Chemicals, Peptides, and Recombinant Proteins		
Blebbistatin	SelleckChem	Cat#S7099
Cytochalasin D	Sigma	Cat#C2618
Doxycyclin	Sigma	Cat# D9891
Monastrol	SelleckChem	Cat#S8439
Nocodazole	Sigma	Cat#M1404
Y27632	SelleckChem	Cat# S1049
QC Colloidal Coomassie Stain	Bio-Rad	Cat#1610803
Experimental Models: Mammalian Cell Lines		
HEK293T	ATCC	Cat#CRL-11268; RRID: CVCL_1926
HeLa	ATCC	Cat# CCL-2; RRID: CVCL_0030
IMCD3	ATCC	Cat#CRL-2123; RRID: CVCL_0429
IMCD3 sgBicc1; tetO::GFP-Bicc1; rtTA	this paper	N/A
Experimental Models: Organisms/Strains		
Mouse strain C57BL/6	Rothé et al., 2015[10]	RRID:MGI:2159769
Recombinant DNA		
pCMV-SPORT6::HA-Bicc1	Maisoneuve et al., 2009	N/A
pCMV-SPORT6::HA-Bicc1 ΔKH	Maisoneuve et al., 2009	N/A
pCMV-SPORT6::HA-Bicc1 ΔSAM	Maisoneuve et al., 2009	N/A
pCMV-SPORT6::HA-Bicc1 mutD	Rothé et al., 2015[10]	N/A
pCMV-SPORT6::HA-Bicc1 ΔKH-mutD	this paper	N/A
pCMV6-Entry::ANKS3-Flag	Origene	Cat#RC223862
pcDNA6::V5-ANKS6	Pr. S. Lienkamp, Hoff et al., 2013[32]	N/A
pCMV-GFP::Bicc1	this paper	N/A
pCMV-GFP::HA-Bicc1	this paper	N/A
pCMV-GFP::HA-Bicc1 ΔKH	this paper	N/A
TRE3G-eGFP-Bicc1-puro	this paper	N/A
hPGK-rtTA3G-IRES-bsd	Pr. David Suter, EPFL	N/A
pCS-Luc::12xMS2	this paper	N/A
pCS-Luc::Dand5-3′UTR-12xMS2	this paper	N/A

Continued

REAGENT or RESOURCE	SOURCE	IDENTIFIER
pCMV-GFP::Bicc1-12xMS2	this paper	N/A
UbiC::NLS-HA-2xMCP-HALO	Addgene, Halstead et al., 2015[42]	Cat#64540
pGEX-1λT::Bicc1	this paper	N/A
pGEX-1λT::Bicc1-KH	Piazzon et al., 2012[23]	N/A
pGEX-1λT::Bicc1-KH$_1$	this paper	N/A
pGEX-1λT::Bicc1-KH$_2$	this paper	N/A
pGEX-1λT::Bicc1-IVS	this paper	N/A
Critical Commercial Assays		
PrimeSTAR® Max DNA Polymerase	Takara	Cat# R045A
NucleoSpin® Gel and PCR Clean-up	Macherey-Nagel	Cat# 740609.50
Glutathione-Sepharose 4B	GE Healthcare	Cat# GE17-0756-01
HaloTag® TMR G8252 ligand	Promega	Cat#G8252
RNasin	Promega	Cat#PRN2615
Protease inhibitors	Roche	Cat# 11697498001
Phosphatase inhibitors	Sigma	Cat#P0044
jetPEI	Polyplus	Cat#101-40N
Software and Algorithms		
FIJI	Fiji/ImageJ	RRID: SCR_002285; http://fiji.sc
ZEN 2009	Zeiss, EPFL BIOP	RRID: SCR_013672
NIS-Elements software	Nikon	RRID: SCR_014329
Leica Application Suite X	Leica	RRID: SCR_013673
Other		
Odyssey CLx scanner	LI-COR Biosciences	N/A
Inverted Zeiss LSM700 confocal microscope	Zeiss, EPFL BIOP	N/A
Inverted Zeiss LSM710 confocal microscope	Zeiss, EPFL BIOP	N/A
3D NSIM Nikon microscope	Nikon, EPFL BIOP	N/A
Leica SP8 confocal microscope	Leica, EPFL BIOP	N/A
Leica SP8 STED 3X	Leica, EPFL BIOP	N/A

RESOURCE AVAILABILITY

Lead contact

Further information and requests for resources and reagents should be directed to and will be fulfilled by the lead contact, Daniel B. Constam (Daniel.Constam@epfl.ch).

Materials availability

All reagents generated in this study are available from the lead contact with a completed Materials Transfer Agreement.

Data and code availability

- All the data reported in this article are available in the supplementary file Data S1.

- This article does not report original code.

- Any additional information required to reanalyze the data reported in this article is available from the lead contact upon request.

EXPERIMENTAL MODEL

IMCD3 (CRL-2123), HEK293T (CRL-11268) and HeLa cell lines (CCL-2) were purchased from ATCC and cultured in DMEM (Sigma) supplemented with 10% FBS (Sigma), 1% GlutaMAX (Thermo Fisher Scientific), and 1% gentamicin (Thermo Fisher Scientific). IMCD3 sgBicc1; tetO::GFP-Bicc1; rtTA cells were derived from the CRISPR/Cas9-edited IMCD3 sgBicc1 clone #14[15] by stable transduction with hPGK-rtTA3G-IRES-bsd and, after selection in blasticidin, transduced with TRE3G-eGFP-Bicc1-puro lentivirus at low MOI and plated at limiting dilution to derive clonal cell lines.

METHOD DETAILS

Antibodies

Monoclonal rabbit anti-HA (Sigma H6908) and mouse anti-FLAG® M2 (Sigma F3165), anti-γ-tubulin (Sigma T6557), and polyclonal rabbit anti-ANKS6 (Sigma HPA008355), and rabbit anti-GAPDH (Abcam ab70699) antibodies were used for Western-blot and/or immunofluorescent staining. Detection of endogenous Bicc1 by Western-blot was performed using custom-made affinity-purified polyclonal rabbit anti-Bicc1 antibody.[10] Detection of endogenous Bicc1 by immunofluorescent staining was performed using a polyclonal rabbit anti-Bicc1 antibody (Sigma HPA045212).

Plasmids

The pCMV-SPORT6::HA-Bicc1, ΔKH, ΔSAM[9] and mutD,[10] pcDNA6::V5-ANKS6,[32] pCMV6-Entry::ANKS3-Flag, pCMV6-Entry::ANKS3ΔCter-Flag[19] and pGEX-1λT::Bicc1-KH[23] have been described previously. PCR fragments of individual KH domains have been amplified from appropriate pCMV-SPORT6 constructs and cloned between BamHI and XhoI sites of pGEX-1λT. To derive pCMV-SPORT6::HA-Bicc1 ΔKH-mutD, a BstBI-XbaI fragment of pCMV-SPORT6::HA-Bicc1 mutD[10] was used to replace the corresponding fragment in pCMV-SPORT6::HA-Bicc1 ΔKH. Plasmid pCMV-GFP::Bicc1 was constructed by cloning the AgeI-XbaI insert of pCMV-SPORT6::HA-Bicc1 including its 3'UTR into XmaI-XbaI sites of pCMV-EGFP-C1(Neo). The ΔKH derivative has been obtained by replacing the internal BsrGI/XmaI fragment encoding Pro_{41}-Gly_{451} by a synthetic linker. Alternatively, to express GFP-Bicc1 without HA tags, Bicc1 cDNA including a 5'UTR of 19 bp was fused to GFP in pCMV-GFP-C1 as an AgeI-XbaI fragment derived from the Bicc1 IMAGE clone 2655954 (Genbank AF319464). To obtain the plasmid pCMV6-Entry::ANKS3Δnter-Flag, a PCR fragment lacking the sequence encoding amino acids 2-220 has been cloned between the KpnI and HindIII sites. To generate doxycycline-inducible TRE3G-eGFP-Bicc1-puro, HA-tagged GFP-Bicc1 from pCMV-GFP::Bicc1 was cloned as an AgeI-XbaI fragment into XmaI-XbaI of a derivative of pLenti CMVTRE3G Puro DEST (w811-1) lacking the Gateway cloning site (provided by David Suter, EPFL, together with lentiviral plasmid hPGK-rtTA3G-IRES-bsd. The plasmid pCS+::AC6-3'UTRprox[23] was used as template for in vitro transcription of the AC6 3'UTR, as described in.[25] To generate pCS-Luc::Dand5-3'UTR, a fragment encompassing the 3'end of the CDS (from nucleotide 539) and the 3'UTR of Dand5 was amplified by PCR and inserted into XhoI and BglII sites of plasmid pCS-Luc-link-MS2 between its firefly luciferase cassette and 3 repeats of the sequence AAAACATGAGGATCACCCATGTCT (MS2 hairpin is underlined). To increase the number of MS2 repeats, the 3 MS2 hairpins in pCS-Luc-link-MS2 were excised by XhoI/HpaI-digestion and replaced by 6 copies of the synthetic sequence ACATGAGGATCACCCATGTCTCTGCAGTCGATAAAGAAAACATGAGGATCACCCATGTCTCTGCAGTCGACTAAAA (GeneArt Gene Synthesis, ThermoFisher) to derive pCS-Luc::12xMS2 control plasmid. Insertion of this synthetic 12xMS2 into BglII-SnaBI of pLuc::Dand5-3'UTR or into the XbaI site of pCMV-GFP::Bicc1, respectively, gave rise to pCS-Luc::Dand5-3'UTR-12xMS2 and pCMV-GFP::Bicc1-12xMS2. UbiC::NLS-HA-2xMCP-HALO was from Addgene.[42]

Plasmid transfection and cell treatment

To induce GFP-Bicc1 and analyze its condensation in the cytoplasm or in cell extracts, IMCD3 sgBicc1; tetO::Bicc1; rtTA cells were treated with 0.5 μg/mL doxycycline for 24 hrs, or as indicated. To assess effects on GFP-Bicc1 mobility, cells were treated with blebbistatin (SelleckChem, 50uM for 30min), cytochalasin D (Sigma, 0.5 M for 1h), monastrol (SelleckChem, 100 μM for 12h), Y27632 (SelleckChem, 10 μM for 2h) or nocodazole (Sigma, 100 ng/ml for 12h). To deplete ANKS3, IMCD3-sh::ANKS3 cells[36] were treated with 0.25 μg/mL doxycycline in fresh complete medium that was renewed every 48 hrs for 8 days.

Purification of GST fusion proteins

Fusions of glutathione S-transferase (GST) with Bicc1 fragments in plasmid pGEX-1λT were expressed in E. coli BL21 (Novagen) as described.[23] Purification was performed using glutathione-Sepharose 4B

(GE Healthcare) according to manufacturer instructions. The beads were resuspended in a buffer consisting of 50 mM Tris-HCl, pH 8, 200 mM NaCl, 1 mM dithiothreitol (DTT).

Sedimentation of membraneless compartments by stepwise differential centrifugation

HEK293T were transfected with 2 μg HA-Bicc1 or HA-Bicc1 ΔKH, or 4 μg HA-Bicc1 ΔSAM per 10 cm dish using jetPEI (Polyplus Transfection) 1 d before the experiment. Transfected HEK293T cells, or stable IMCD3 sgBicc1; tetO::GFP-Bicc1; rtTA cells (one 10 cm dish per condition) were washed with ice-cold PBS and passed eight times through a syringe needle (no. 30) in extraction buffer containing 50 mM Tris-HCl (pH 7.6), 5 mM MgCl$_2$, 50 mM NaCl, 1 mM dithiothreitol (DTT), 0.1% Nonidet P-40 (NP-40), Rnasin (Promega), phosphatase inhibitors (Sigma), and protease inhibitors (Roche). After a first centrifugation at 2,000 g for 2 min at 4°C, the extracts were centrifuged by steps of increasing speed from 4,000 g to 10,000 g for 5 min at 4°C each. After gentle collection of the supernatants, the pellets were resuspended after each step in the same volume of extraction buffer as the initial cell pellet. To assess whether GFP-Bicc1 sedimentation is salt-sensitive, aliquots of the supernatant of a 4,000 g centrifugation were supplemented with increasing concentrations of NaCl and incubated for 20 min at 4°C before sequential centrifugation at 4,000 g and 10,000 g. Alternatively, to assess whether the sedimentation in heavy fractions depends on RNA, supernatants from a 4,000g centrifugation were incubated for 20 min at RT with 0.4 μg/μL of Rnase A or with 15 pmol of *in vitro* transcribed RNA prior to centrifugation at 10,000 g. For Western blot analysis of heavy and light fractions, 15 μl aliquots of each were dissolved in Laemmli buffer, size-separated on reducing SDS PAGE gels, transferred to nitrocellulose membranes, blocked with skim milk and incubated over night with the indicated antibodies, and with fluorescently labelled secondary antibodies for analysis on an Odyssey CLx scanner (LI-COR Biosciences).

Protein co-immunoprecipitation assay in HEK293T cells

HEK293T cells were transfected with 2 μg GFP-Bicc1, HA-Bicc1 or HA-Bicc1 ΔKH per 10 cm dish, or with 4 μg HA-Bicc1 mutD or HA-Bicc1 ΔKH-mutD. 24 hrs later, cells from two dishes per condition were washed with ice-cold PBS and pooled in extraction buffer containing 20 mM Tris-HCl (pH 7.4), 2.5 mM MgCl$_2$, 100 mM NaCl, 5% glycerol, 1 mM dithiothreitol (DTT), 0.05% Nonidet P-40 (NP-40), Rnasin (Promega), phosphatase inhibitors (Sigma), and protease inhibitors (Roche). Total cell extracts were prepared by ultrasonication followed by two rounds of centrifugation at 10,000 × g for 5 min at 4°C to remove debris. Supernatants were incubated with anti-HA beads (Sigma) for 2 hrs at 4°C on a rotating wheel. After washing four times for 10 min in 20 mM Tris-HCl pH 7.4, 2 mM MgCl$_2$, 200 mM NaCl, 1 mM DTT, and 0.1% NP-40, beads were suspended in Laemmli buffer and loaded on reducing SDS PAGE gels to size-separate eluted proteins. For immunoblot analysis, proteins were transferred to nitrocellulose membranes, blocked with skim milk and incubated over night with the indicated antibodies, and with fluorescently labelled secondary antibodies for quantitative analysis on an Odyssey CLx scanner (LI-COR Biosciences) that has a high dynamic range and automatically flags and excludes saturated bands.

Reconstitution of multiprotein complexes and RNP by GST pull-down

To assess binding of GST-Bicc1 fusion proteins to HA-Bicc1 WT, ΔKH or ΔSAM, HEK293T cells were transfected and extracted as described above. Cleared extracts were incubated for 2 hrs at 4°C with glutathione-Sepharose 4B beads that were coated with GST alone (control), or with GST-Bicc1 fusions. Proteins that were bound to the beads were washed and analyzed by Western blotting as described above. Retention of the GST fusions was validated by Coomassie staining of eluted proteins.

Tracking of GFP Bicc1 granules

After treatment with 1 μg/mL doxycycline for 24 hrs on 35 mm glass bottom plates (Ibidi), IMCD3 sgBicc1; tetO::GFP-Bicc1; rtTA cells were placed in PBS and imaged at 37°C using a TCS SP8 STED 3x microscope (Leica Microsystems) equipped with white-light laser. Images were acquired using a 63x objective with a 7.5x optical zoom and pinhole size of 5 Airy Units (AU). Image format and laser speed were set at 512 x 512 pixels and 1400, respectively. Images were taken every 15 seconds intervals for 15 min along the Z-axis. Time-lapse videos were generated after Z-projection (maximum intensities) of all images. Dynamic parameters were obtained using ImageJ TrackMate plugin and R statistical software. The parameters to extract Links, Spots and Tracks statistics from Trackmate were as follows: Estimated blob diameter, 0.6 μm; Filter spots, "Mean intensity"; Linking Max Distance, 2 μm; Gap-closing max distance, 1 μm; Gap-closing max frame gap, 0 μm. For a given recording, individual spot displacement values were

normalized based on the track length, which corresponds to the number of consecutive images where a spot was successfully tracked.

Classification of GFP-Bicc1 condensates by their shapes, and quantification of mRNA co-localization

The size and circularity of protein condensates were measured using the Analyze Particles tool of Image J. The Watershed algorithm was used to separate particles in close contact. Condensates were binned into four distinct categories. The category "Regular granules" corresponds to non-fibrillar condensates in the range of size of 0.05 to 3 μm^2, as observed for endogenous Bicc1 in mouse kidney (Fig. S3E). The category "Enlarged condensates" corresponds to non-fibrillar condensates larger than 3 μm^2. The categories "Fibrils" and "Granules with fibrillar connections" comprise the cells harboring fibrillar condensates alone or together with regular granules smaller than 3 μm^2, respectively. The Mander's coefficient as an estimate of the co-localization of GFP-Bicc1 and mRNA condensates was calculated using the JACoP BIOP plugin (available on Fiji upon installation of PTBIOP and IBMP-CNRS update sites).

FRAP analysis

FRAP analysis in HeLa cells was performed using a Zeiss LSM710 confocal microscope with a 63x/0.9NA lens. ROI were photobleached with maximum laser power at 488 nm or 561 nm wavelengths. Images were taken during 4 min at 2.5 sec (GFP-Bicc1) or 0.2 sec (TMR) intervals with a fully open pinhole. The laser power was set in a range of 0.15-8%, the gain was optimized for each z-stack in a range of 400-800 to avoid saturation, and the pixel dwell time was set at 1.27 μsec. Results were expressed as the percentage of recovery relative to the baseline of residual fluorescence intensity after photobleaching at t = 0 sec, and normalized to the fluorescence of an unbleached area. The half-time of recovery was estimated by linear regression.

Structured illumination microscopy

HeLa cells on cover slips with a thickness of 170 μm were transfected with 1 μg of plasmid per well in a 6-well plate. After 24 hrs, cells were fixed in methanol for 10 min at -20°C and imaged on a 3D NSIM Nikon microscope using an objective APO TIRF100x/1.49 oil combined with an additional lens 2.5x. GFP-Bicc1 was detected using a Coherent Sapphire 488 nm laser (200 mW) and imaged using an Andor iXon3 897 camera. The acquisition time was 100 ms at a readout of 3 MHz. 3D images were reconstructed from stacks of 15 images (5 phase shifts and 3 rotations) with a z-step of 120 nm. Pictures of the final 3D volume rendering were generated using Imaris software.

Immunofluorescence staining

HeLa cells transfected with 1 μg of plasmid per well in 6-well plates were incubated and one day later passed to sterile coverslips in 24-well plates. After incubation for another day, cells were fixed in methanol for 10 min at -20°C. After washing in PBS, coverslips were incubated 1 hr at RT in blocking buffer containing PBS and 1% BSA, and 2 hrs at RT in blocking buffer containing appropriate combinations of the following antibodies, as indicated in the figures: anti-Bicc1 (1/200, Rabbit, Sigma), anti-HA (1/500, Rabbit, Sigma), anti-Flag (1/500, mouse, monoclonal clone M2, Sigma) and/or anti-ANKS6 antibodies (1/500, Rabbit, Sigma). After rinsing with PBS, cells were incubated with anti-mouse Alexa 568 and/or anti-rabbit Alexa 647 in blocking buffer for 1 hr at RT in presence of DAPI (1/10000). For cryosectioning, kidneys were collected and prepared from C57BL/6 mice as described in.[10] Pictures were acquired on a Leica SP8 confocal microscope with a 63x/1.4NA lens. The laser power was set in a range of 1-2%, the gain was optimized for each image in a range of 400-800 to avoid saturation, the pinhole size was set at 1 Airy Unit, and the pixel dwell time was set in a range of 0.8 to 3.2 μsec.

Protein-RNA colocalization by time-lapse imaging

3×10^5 HeLa cells in 35 mm glass bottom dishes (Ibidi) were transfected with 2xMCP-NLS-HaloTag together with GFP-Bicc1-12xMS2 (1 μg each) or, where indicated, with GFP-Bicc1 and either Luc-12xMS2 or Luc-*Dand5 3'UTR*-12xMS2 reporters. After 36 hrs, cells were incubated for 15 min with the HaloTag® TMR G8252 ligand (Promega) in fresh medium. Thereafter, unbound TMR was removed by washing 3 times with culture medium (including a final incubated incubation in fresh medium for 30 min) and 3 times in PBS. Imaging was performed in PBS supplemented with 2% BSA on an inverted Zeiss LSM700 confocal microscope with a 63x/1.4NA lens. The laser power was set in a range of 2-10%, the gain was optimized for

each z-stack in a range of 400-800 to avoid saturation, the pinhole size was set at 1 Airy Unit, and the pixel dwell time was set in a range of 0.4 to 0.8 μsec. Four stacks were acquired every 1.5 min during at least 15 min. Videos were mounted with a speed of 5 pictures/sec.

QUANTIFICATION AND STATISTICAL ANALYSIS

Images were analysed using ImageJ software in Fiji. Western blot signals were quantified using the Odyssey CLx scanner software ensuring that all bands were below saturation. Statistics were calculated with the Microsoft Excel software. Error bars represent standard deviations (SD). Student's *t* test was used to calculate p values, with $p \leq 0.05$, $p \leq 0.01$ or $p \leq 0.001$ represented by one, two or three asterisks, respectively. Statistical details of individual experiments can be found in the figure legends and in the Data S1 file.